Porous-Organic-Polymer-Triggered Advancement of Sustainable Magnetic Efficient Catalyst for Chemoselective Hydrogenation of Cinnamaldehyde

Ratul Paul,[a] Chitra Sarkar,[a] Yong Yan,[b],[c] Quang Thang Trinh,[c] Bolla Srinivasa Rao,[a] Chih-Wen Pao,[d] Jyh-Fu Lee,[d] Wen Liu,[b],[c] and John Mondal*[a]

[a] R. Paul, C. Sarkar, B. S. Rao and Prof. Dr. J. Mondal
Catalysis & Fine Chemicals Division, CSIR-Indian Institute of Chemical Technology, Uppal Road, Hyderabad-500007, India.
Email: johncuchem@gmail.com; johnmondal@iict.res.in

[b] Dr. Y. Yan, Prof. W. Liu
School of Chemical and Biomedical Engineering, Nanyang Technological University, 62 Nanyang Drive, Singapore 637459.
[c] Dr. Q. T. Trinh
Cambridge Centre for Advanced Research and Education in Singapore (CARES), Campus for Research Excellence and Technological Enterprise (CREATE), 1 Create Way, 138602, Singapore.
[d] Dr. C. W. Pao, Dr. J. F. Lee
National Synchrotron Radiation Research Center, 101 Hsin-Ann Road, Hsinchu 30076, Taiwan.

Abstract: Intriguing characteristics including high specific surface area, adjustable chemical functionality, flexibility of molecular design, high hydrothermal and mechanical stability of Porous-Organic-Polymers (POPs) present new opportunities for them to become a versatile platform in heterogeneous catalysis. Cinnamaldehyde (CAL), a representative α,β-unsaturated aldehyde, is an essential molecule, because its partially hydrogenated products, namely cinnamyl alcohol (COL) and hydrocinnamaldehyde (HCAL) are key intermediates for the production of fine chemicals including perfumes, flavorings and pharmaceuticals. In this study, we adopted a cost-effective, facile and metal & template-free strategy for the successful synthesis of hydroxyl enriched POP (denoted as TPT). The TPT was prepared by the simple one-pot condensation of triphenyl amine and terephthaldehyde in the presence of *p*-toluene sulphonic acid, which served as an organic catalyst. Accordingly, an integrated catalyst, Pd-Fe_3O_4@TPT, has been developed for the liquid phase selective hydrogenation cinnamaldehyde (CAL). Pd-Fe_3O_4@TPT exhibited excellent catalytic performance, providing 100% selectivity towards hydrocinnamaldehyde (HCAL) under mild reaction conditions (with relatively low hydrogen pressure and very short reaction time), whereas Fe_2O_3@TPT appeared inert. Compared with the conventional catalytic

systems, our newly designed catalyst was superior in many aspects, owing to the rigid nature of TPT-POP, which prevents aggregation and leaching of the metal nanoparticles. We identify Pd nanoparticles (-NPs) to have two decisive roles, namely (I) transformation of Fe_2O_3 to Fe_3O_4 through metal-support interaction and (II) triggering the catalytic activity. A decrease in the Pd-Pd bond distance (~2.7 Å to ~2.49 Å) along with the shift of Fe K-edge to a lower energy was observed by the synchrotron EXAFS analysis of Pd-Fe_3O_4@TPT, revealing that Pd facilitated the reduction of Fe_2O_3 to Fe_3O_4. The significant enhancement in catalytic performance for the selective hydrogenation of C=C over C=O bond could be ascribed to the flat adsorption of C=C over the Pd surface and C=O bond shortening, as suggested by in-situ ATR-IR and DRIFTS spectroscopy studies. Density Functional Theory (DFT) calculations reveal two possible ways by which TPT-POP could contribute to the highly selective hydrogenation of C=C bond on the Pd-Fe_3O_4@TPT catalyst. Firstly, TPT acts as a structural template for generating highly concentrated Pd step sites and other low coordinated sites, which possess high activity towards C=C bond hydrogenation. Secondly, the charge transfer from TPT to the Pd clusters increases the negative charge density of the Pd sites, consequently enhancing their C=C hydrogenation activity. The present findings provide new inspirations for designing easily realizable, low-cost, and high performance catalysts for sustainable chemistry via effective surface/interface engineering.

Keywords: *Porous-Organic-Polymer*, *Cinnamaldehyde hydrogenation*, *Terephthaldehyde*, *Magnetic Nanocatalyst*, *Density Functional Theory (DFT) calculations.*

Introduction

Chemoselective hydrogenation of C=C and, or C=O in α,β-unsaturated aldehydes is an indispensable approach in fine chemical manufacturing. Cinnamaldehyde (CAL), a representative α,β-unsaturated aldehyde, is an industrially important molecule, because its partial hydrogenation products, viz. cinnamyl alcohol (COL) and hydrocinnamaldehyde (HCAL) are key intermediates for the synthesis of high-value products, including perfumes, flavorings and pharmaceuticals.[1-3] For example, HCAL is demonstrated to be an important intermediate in the formulation of a HIV drug.[4] Cinnamaldehyde (α,β-unsaturated aldehyde), a typical model

component representing the coniferyl aldehydes and sinapaldehydes derived from lignin-, could be produced by electron abstraction of the phenoxy radicals followed by disruption of the C_α-C_β bond through retro-aldol cleavage of lignin.[5] Therefore, lignin-derived chemicals can serve as platform molecules towards the production of a wide range of value-added chemicals, whose implementation will motivate the transformation towards a sustainable chemical industry.

With the advancing knowledge and developments in the field of engineering heterogeneously supported metal catalysts for diverse chemical applications, various research groups reported that Pt,[6]Au,[7] Ru,[8] Ir,[9] Co,[10]and Cu[11] based supported metal catalyst are active for the selective hydrogenation of CAL to COL. Liu and coworkers discovered that Pd metal supported on multi-walled carbon nanotube is an active catalyst for the selective hydrogenation of cinnamaldehyde to saturated aldehyde, showing 91.3% selectivity under 40 bar H_2 and 148 bar CO_2 partial pressure at 60 °C.[12] Pd nanoparticles deposited on N-doped mesoporous carbon is also an effective catalyst for producing partially hydrogenated HCAL with 93% selectivity under low H_2 pressure at room temperature.[13] Remarkably, Wei *et al.* reported that Co based inter-metallic compounds, derived from layered double hydroxide, exhibited 96% selectivity towards cinnamyl alcohol.[14] By evaluating the sustainability and greenness of selective hydrogenation reaction, Kubo *et al.* reported boronate micro-particle supported nano palladium and nano gold catalyst for the chemoselective reduction of C=C and C=O bonds of cinnamaldehyde, respectively, using environmentally benign solvents.[15] Recently, Hu *et al.* established the strategy of using metal organic frameworks (MOFs) and metal nanoparticles shelled structures e.g. MOFs@NPs@MOFs for the partial hydrogenation of CAL with 97.3% selectivity towards cinnamyl alcohol, with an elevated turn over frequency to 1516.1 h^{-1}.[16] A distinct class of porous materials have been fabricated by combining porous Pt-Ni nano-wires and MOFs to intensify the catalytic activity for producing cinnamyl alcohol with 83.3% selectivity.[17] Indeed, Yang *et al.* recently employed water as a hydrogen exchange bridge over carbon nanotube supported bimetallic Pt-Fe catalyst for the successive synthesis of partially hydrogenated cinnamyl alcohol from cinnamaldehye.[18] Although all the accomplished work on the partial reduction of cinnamaldehyde report good selectivity along with high conversion, there remain challenges associated with catalyst recyclability, leaching of metal nanoparticles and the high cost of noble metals.

To address the above challenges, some researchers have started exploring the material space of micro porous polymeric network with functional building blocks,[19] such as covalent organic frameworks(COFs),[20] polymers with intrinsic micro porosity (PIMs),[21] conjugated micro porous polymers (CMPs),[22] hyper-cross-linked polymers (HCPs),[23] porous organic polymers (POPs),[24] covalent triazene frameworks (CTFs)[25] and covalent molecular organic cage (MOC),[26] owing to their high thermal and chemical stability,[27] excellent surface hydrophobicity,[28] low skeletal density, and large specific surface area. Amongst the various synthetic approaches available for preparing hyper-cross-linked porous organic network, acid catalyzed condensation polymerization is the most suitable for constructing a ameliorate polymeric backbone with -OH functional groups, which are readily available for further modification.

With these considerations, we report herein a truly cost-effective facile, metal-free, and template-free synthetic strategy to develop -OH group functionalized Porous-Organic-Polymer (TPT) *via* the one-pot condensation of triphenyl amine and terephthaldehyde. This synthetic strategy avoids the use or generation of substances that are toxic to humans and,or the environment. Our research aligns with the globally emerging interest in developing environmentally benign, sustainable, and low-metal consumption chemical synthesis processes.[29]Also, the one pot synthesis method used involves the incorporation of all the raw materials into the final product, thereby facilitating atom economy. Specifically, we demonstrate this simple method for the synthesis of diphenyl-methanol bearing, magnetic monohybrid catalyst, *viz*. Pd-Fe_3O_4@TPT, which could be implemented effectively for the catalytic chemoselective hydrogenation of cinnamaldehyde (CAL) to hydrocinnamaldehyde (HCAL), with preference to attack the conjugated C=C group, whilst leaving the C=O bond untouched. Through polymerization, the diphenylmethanol based TPT-POP framework may provide higher proportion of active surface sites for enhanced catalytic activity and strengthened catalyst durability. Here, functionalized and magnetically retrievable catalysts mitigate the needs for complex catalyst recovery steps (e.g. filtration and repeated washing) at the end of the reactions, thus providing cost-effective, energy efficient and sustainable pathways for the catalytic conversion of chemical feedstocks.[30] The evolution of catalytic efficiency and structure-activity relationship have been established based on comprehensive characterization results, including wide-angle powder X-ray diffraction (XRD), N_2physisorption, ^{13}C cross-polarization (CP) solid-

state magic angle spinning (MAS), nuclear magnetic resonance (NMR), Fourier transform infrared (FT-IR), X-ray photoelectron spectroscopy (XPS), high-resolution transmission electron microscopy (HR-TEM), field emission scanning electron microscopy (FE-SEM), energy dispersive X-ray (EDX) mapping, extended X-ray absorption fine structure (EXAFS), attenuated total reflectance-infrared spectroscopy (ATR-IR), and diffusive reflectance infrared Fourier transform spectroscopy (DRIFT). The remarkable electronic metal-support interaction (EMSI), which modulates the local atomic structure and electronic environment of the Pd-Fe_3O_4 interface, brings unique synergies that promote the catalytic activity, selectivity and stability of the Pd-Fe_3O_4@TPT catalyst.

EXPERIMENTAL SECTION

Materials

Triphenylamine, terepthaldehyde, palladium acetate ($Pd(OAc)_2$), ferric chloride ($FeCl_3$), polyvinyl pyrrolidone (PVP), *p*-toluene sulphonic acid were purchased from Sigma-Aldrich and used as received unless noted otherwise. 1,2-dichlorobenzene, ethylene glycol and methanol solvents were all dried before using in reactions.

Synthesis of Porous-Organic-Polymer (TPT):

Porous organic polymer (TPT-POP) was synthesized through typical one-step condensation polymerisation in a sealed tube under high vacuum condition, p-toluene sulphonic acid and dichlorobenzene were added as catalyst and solvent, respectively, with a slight modification from the previous report.[31] In a typical synthesis, triphenylamine (1.0 mmol, 245 mg), terephthalaldehyde (1.5mmol, 201mg) and *p*-toluene sulphonic (290 mg) acid were first charged into a 25 ml sealed tube, followed by the addition of 1,2-dichlorobenzene (5 ml). To ensure the complete dispersion of all the reactants in the solvent, the reaction mixture was sonicated in an ultrasound bath for 30 mins. The well-dispersed solution was then degassed by three freeze-pump-thaw cycles at 77 K using liquid N_2. Next, the tube was flame sealed and kept in an oven at 150 °C for 12 hours. After cooling to room temperature, the bluish-green solid was collected and washed thoroughly with methanol, acetone, dichloromethane, and THF, respectively. Finally, the solid product was dried overnight in a vacuum oven at 100 °C .

Synthesis of Fe_2O_3@TPT and Pd-Fe_3O_4@TPT:

At first, the as-synthesized 150 mg TPT-POP was dispersed in ethylene glycol (30 ml), followed by the addition of a solution of polyvinyl pyrrolidone (PVP, 25 mg) in ethylene glycol (5 ml) and water (5 ml). The reaction mixture was kept stirred for at least two hours. Then, a solution of $FeCl_3$ (0.567 mmol, 92 mg) in ethylene glycol (10 ml) was prepared and added drop-wise into the previous mixture under constant stirring. After two hours, the resulting mixture was taken into an autoclave and heated at 150 °C for 8 hours. After cooling to room temperature, the brownish-black solid product (Fe_2O_3@TPT) was separated from the mixture by centrifugation and washed with methanol. Finally, the solid product was dried overnight in vacuum at 80 °C. For the preparation of the black colored Pd-Fe_3O_4@TPT, we added $PdCl_2$ (0.189 mmol, 35mg) in the solution of polyvinyl pyrrolidone (25 mg) in ethylene glycol (5 ml) and water (5 ml), then followed the same procedure for the synthesis of Fe_3O_4@TPT.

Catalytic activity for Cinnamaldehyde Hydrogenation:

The catalytic hydrogenation of cinnamaldehyde was performed in a 100 ml Parr autoclave reactor, which is protected by stainless steel shell, fitted with an built-in pressure gauge set up (measuring 0-12 MPa) and a temperature rating of 573K. In a typical experiment, cinnamaldehyde (0.25 ml, 2mmol), along with the catalyst (0.03 g), were dissolved or dispersed in 30 ml isopropanol. The reaction mixture was charged into the reactor. The reactor was then sealed and evacuated using vacuum pump for 15 min at room temperature to remove the dissolved oxygen. The required H_2 pressure of 10 bar was achieved by purging the reactor with pressurized H_2 for at least 10 times. The reaction was conducted for a specified period with continuous stirring at 1000 rpm at the constant temperature of 60 °C. After the completion of the reaction, the reactor was kept aside to cool down. The progress of the reaction was monitored by sampling at regular time intervals and analyzing the product mixtures using an Agilent 6980 gas chromatograph (GC) equipped with a flame ionization detector and an SE-54 capillary column (30 m × 0.32mm × 1.0 μm). During GC analysis, toluene was used as an internal standard with a standard deviation of less than 2%.

RESULTS AND DISCUSSIONS

Catalyst Synthesis and Characterization

The TPT-POP material has been synthesized through organic acid catalyzed, metal & template-free, one-pot condensation of triphenyl amine and terepthaldehyde under sealed-tube conditions to produce a bluish-green solid (Scheme 1). The rate of polymerization towards a 3D cross-linking framework is accelerated in a closed glassware system. The highly active triphenyl amine monomer, each bearing three electron rich phenyl units, contributed to the electrophilic aromatic substitution with two aldehyde groups of terephthaldehyde, where each triphenyl amine molecules could be linked together by their *para* position with two terephthaldehyde units. A huge amount of -OH functional groups in the polymeric backbone, could be found in the resulting TPT-POP. These -OH groups are available for further functionalization. The as-prepared diphenylmethanol based TPT-POP is very stable and insoluble in common organic solvents, attributing to the successful formation of the highly rigid and cross-linked network. To the best of our knowledge, we have utilized condensation-polymerization inspired chemistry to demonstrate the feasibility of our novel approach with rigid aromatic building blocks and external linker based TPT-POP. Sequential synthesis procedure involving solvothermal reduction was employed, where Pd and Fe_3O_4 NPs were homogeneously incorporated in the OH-rich POP framework (designated as Fe_2O_3@TPT& Pd-Fe_3O_4@TPT). Color change from brownish black to intense black was observed during the formation of the Fe_2O_3@TPT and the Pd-Fe_3O_4@TPT nano-hybrid, probably owing to the *in situ* phase transformation from α-Fe_2O_3 to Fe_3O_4, which is mediated by the Pd nanoparticles.

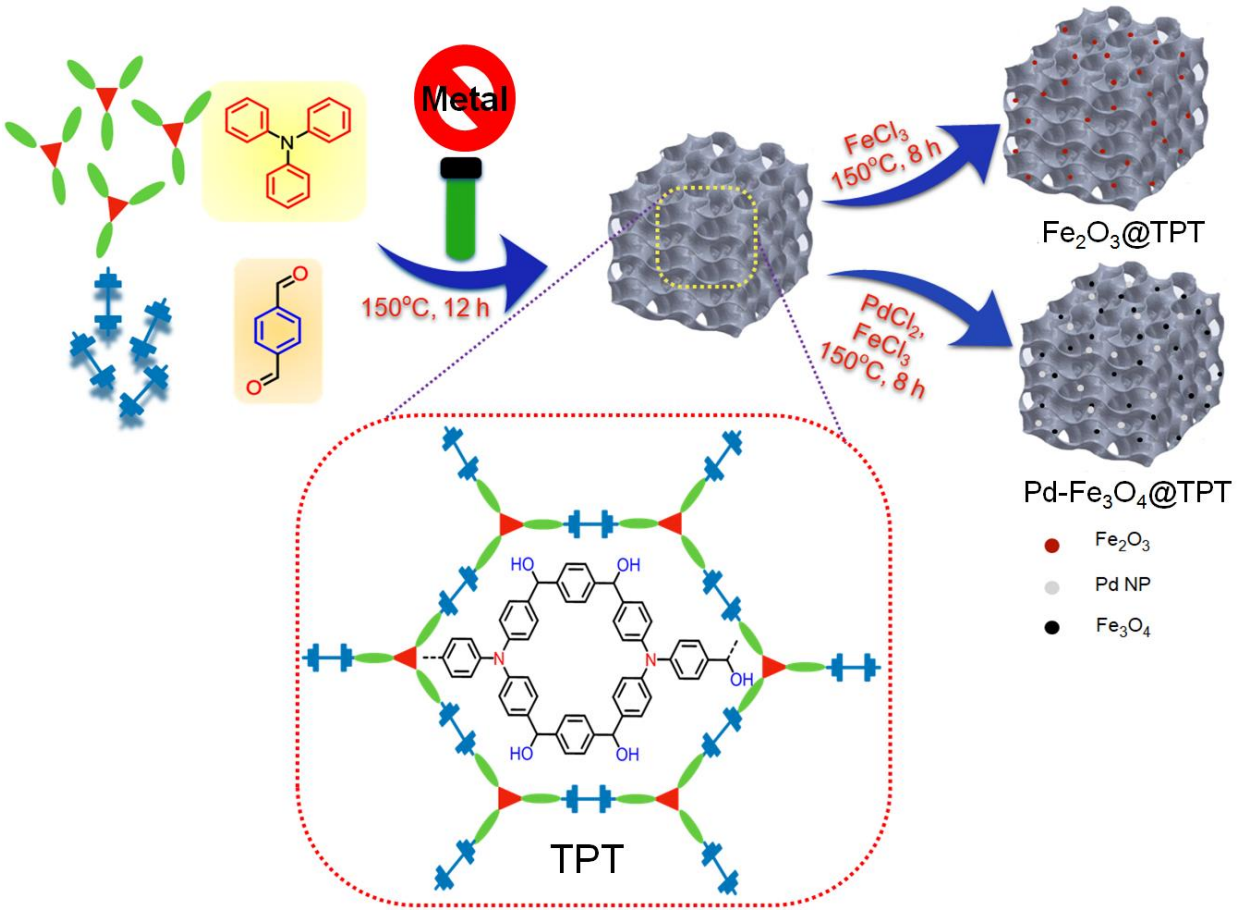

Scheme 1: SchematicIllustration for the synthesis of Porous-Organic-Polymer and the sequential synthetic approach for Pd-Fe_3O_4 based integrated catalyst.

In order to examine the thermal stability of the as-synthesized TPT-POP, TGA experiments were carried out. The prominent decrease of wt% below 100 °C belongs to the loss of water or gas molecules trapped in the organic framework. Distinct weight loss with increasing temperature after 100 °C indicates the release of free -OH groups from the porous skeleton (Figure S2). Furthermore, weight loss continued beyond 400 °C, probably owing to temperature assisted C-C bond cleavage along with burning of organic framework present in the porous organic network. The parent TPT contains 77.28 wt% C, 3.85 wt% H and 2.59 wt% N, as established by elemental (C, H, N) analysis. After the incorporation of iron oxide, the carbon content of Fe_2O_3@TPT and Pd-Fe_3O_4@TPT decreases drastically to 59.61 wt% and 55.04 wt%, respectively, along with the hydrogen content (4.10 and 3.46 wt%, respectively) and the nitrogen content (4.12 and 3.75 wt%, respectively) (Table S1). Pd and Fe contents in the Pd-Fe_3O_4@TPT are 0.173 & 0.285

mmol/g, respectively, as measured by Inductively Coupled Plasma Mass Spectrometry (ICP-MS). ^{13}C CP solid-state MAS NMR spectrum analysis was performed to obtain the molecular connectivity and the chemical environment of the carbon nuclei of the polymeric skeleton of the three as-synthesized porous materials, namely TPT, Fe_2O_3@TPT and Pd-Fe_3O_4@TPT (Figure 1a). We distinguished a common resonance peak for all three samples near 55 ppm, attributed to the tertiary aliphatic carbon-containing hydroxyl group (-OH). The unsubstituted aromatic Sp^2 carbon peak of the as-synthesized TPT polymer appears at 127 ppm, while two peaks at 138 and 144 ppm are ascribed to the C-substituted and N-substituted aromatic carbon. The absence of the aldehyde (-CHO) carbon resonance peak around 190 ppm clearly indicates the complete incorporation of aldehyde groups into the polymer material.[30] In the parent TPT-POP, the sharp peak at 144ppm corresponds to the N-substituted carbon atom of the benzene ring, which has been shifted to the higher values of 146 ppm and 149 ppm for Fe_2O_3@TPT, Pd-Fe_3O_4@TPT, respectively. This alteration in the δ-value could be associated with the intrinsic synergistic effect developed by the *in situ* incorporation of Fe_2O_3 and bimetallic Pd-Fe_3O_4 on the TPT-POP surface, which regulates the electronic environment around the N-atom as a result of the charge transfer from N to Fe and Pd. Therefore, the electron density around the N-atom contracts, and eventually withdraws electrons from the adjacent C-atom, making the latter more de-shielded, hence shifting the peak to a higher δ-value. However, we discriminate some broad peaks near 50 ppm for Fe_2O_3@TPT, probably attributed to the presence of large numbers of hydroxyl groups on the surface of Fe_2O_3, as hydrogen bonding interaction between them can influence the surrounding electronic environment.

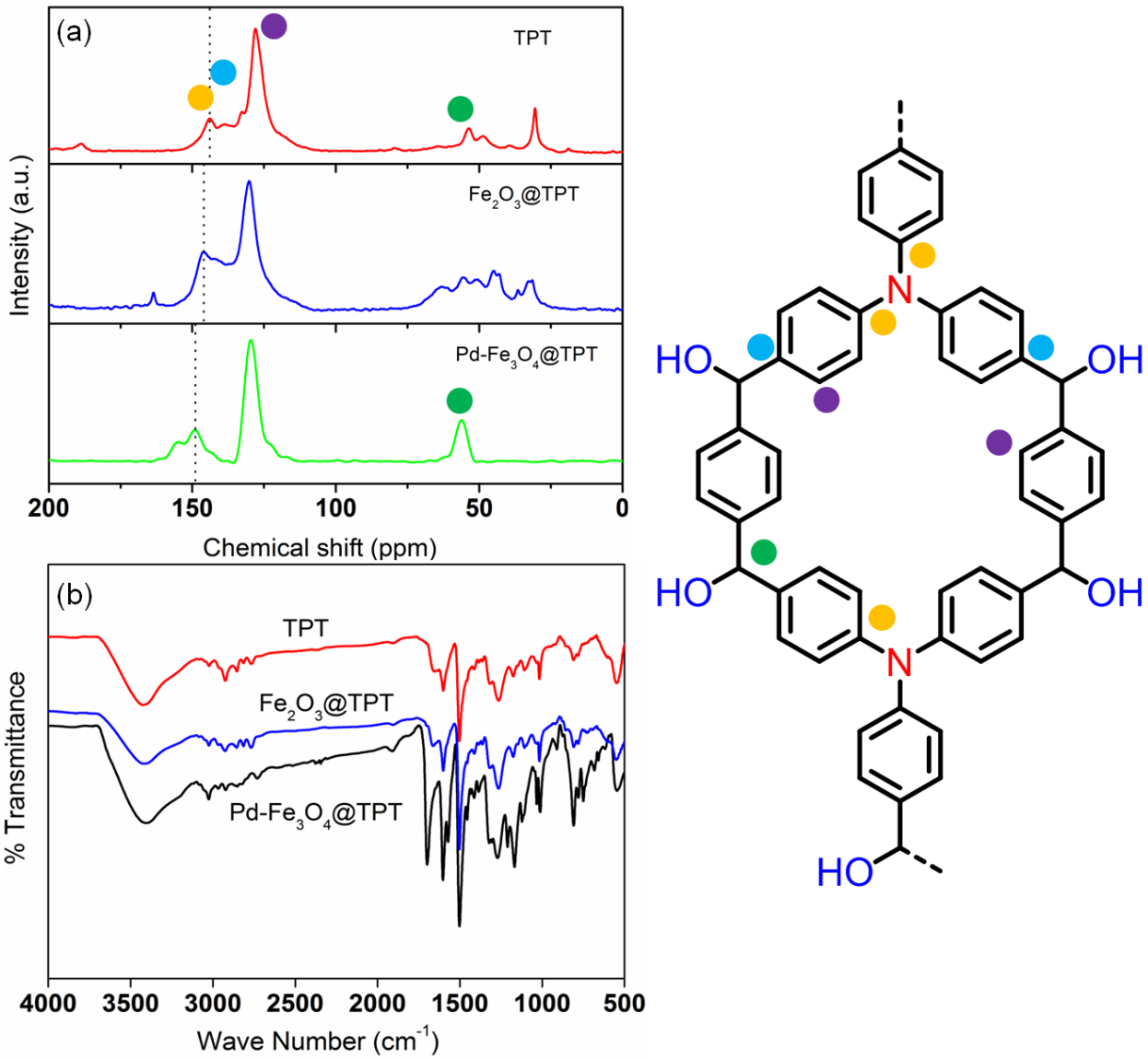

Figure 1: (a) ^{13}C CP solid state MAS NMR spectra, (b) FT-IR spectra of TPT, Fe_2O_3@TPT and Pd-Fe_3O_4@TPT.

The polymeric framework construction with covalent bonding in all the TPT-POP based materials have been elucidated by FT-IR spectroscopy (Figure 1b). A peak around 3420 cm^{-1}, characteristic of hydroxyl functional groups of the porous framework, is observed for the parent TPT as well as the Fe_2O_3@TPT and Pd-Fe_3O_4@TPT nanocomposites.[30] The corresponding $C_{sp}{}^2$-H and $C_{sp}{}^3$-H bond (coupled to the –OH group) frequencies are detected around 3020 cm^{-1} and 2928 cm^{-1}, respectively. C-N stretching peak of triphenyl amine and –COOH of

terepthaldehyde can be seen around 1600-1674 cm^{-1} and 1500 cm^{-1} & 1263-1318 cm^{-1}, respectively, both clearly indicating the fabrication of the porous organic network, in good agreement with previous works.[32,33] In Fe_2O_3@TPT, the formation of α–Fe_2O_3 is confirmed by the characteristic peaks of the Fe-O bond at 547 cm^{-1} and 470 cm^{-1}, whereas for Pd-Fe_3O_4@TPT nano-hybrid, Fe_3O_4 single absorption peak is noticed at 546 cm^{-1} after deposition of iron oxide by solvothermal method.[34] N_2 adsorption-desorption isotherm analysis at 77 K was employed to evaluate the permanent porosity and the specific surface area present on the TPT-POP based materials. The accordingly analyzed pore size distribution curves are presented in Figure 2a & 2c, which shows that the as-synthesized TPT-POP, Fe_2O_3@TPT and Pd-Fe_3O_4@TPT all exhibit behaviors resembling a combination of type I and IV isotherms (according to IUPAC classification), suggesting the dominance of mesopores.[35] The large hysteresis loop at the high pressure region, probably due to the swelling of polymeric units upon gas adsorption and the subsequent elastic deformation of pores and inter-particle voids, made the whole gas adsorption process irreversible in nature. Brunauer-Emmett-Teller (BET) surface areas of TPT-POP, Fe_2O_3@TPT and Pd-Fe_3O_4@TPT are measured to be 532.8 m^2/g, 462.3 m^2/g & 410.7 m^2/g, respectively, with the corresponding pore volumes of 1.593 $cm^3\ g^{-1}$, 1.213 $cm^3\ g^{-1}$ and 1.106 cm^3g^{-1}, respectively. We have observed a diminishment in the BET surface area owing to the accommodation of the NPs inside the porous channel and a mass increment of the parent POP, thereby inhibiting N_2 uptake. Our observation is fully consistent with the previous report by Wang *et.al*.[36] The pore size distribution curve, as derived by the NLDFT (Non-Local-Density-Functional-Theory) fitting of the adsorption branches model (Figure 2c), clearly demonstrates the mesoporous nature of the three as-synthesized materials, with a distinct sharp peak predominately appearing in the 2-3 nm range. We also find a contraction of pore-width from 2.58, 2.4 & 2.07 nm, respectively, which could be attributed to the clogging of the pore-channels by the high density metal NPs.

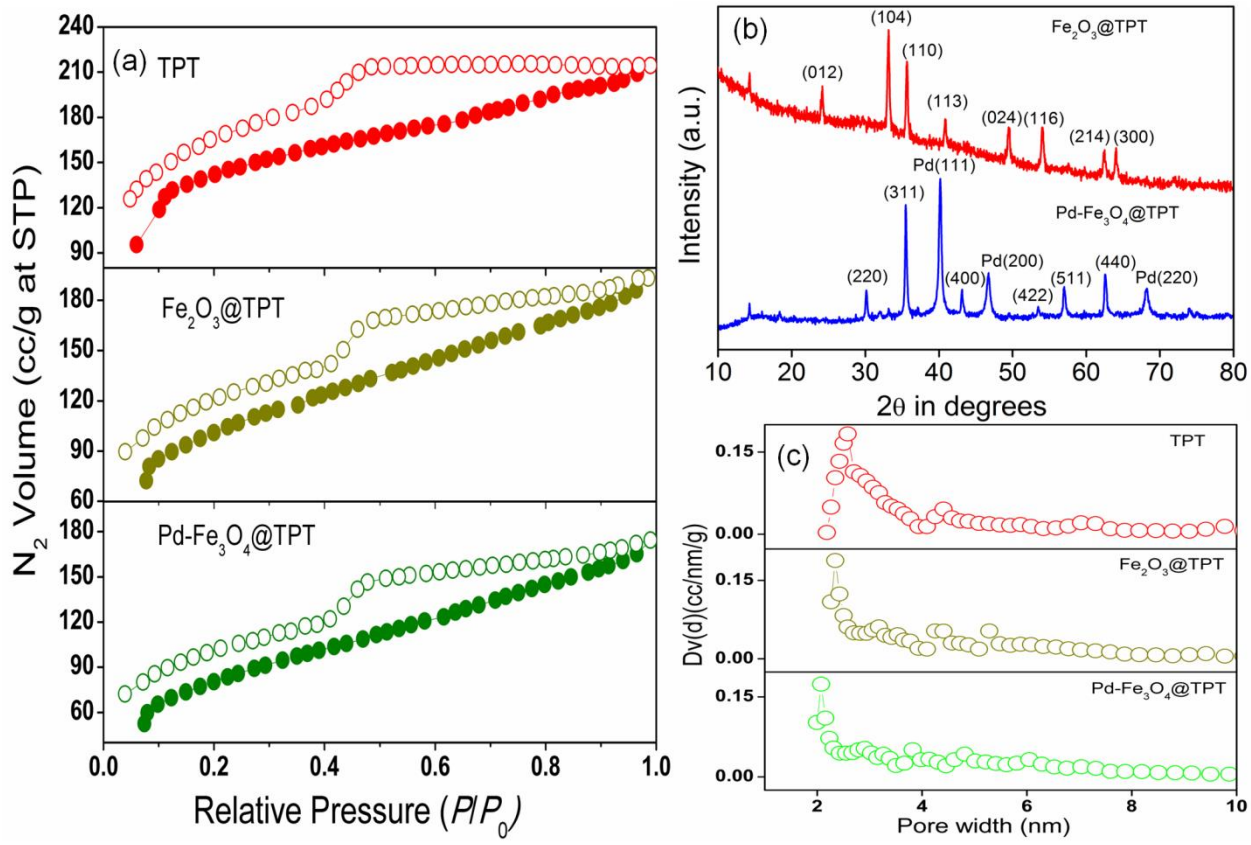

Figure 2: (a) Nitrogen adsorption/desorption isotherms, (b)Wide-angle powder X-ray diffraction patterns,(c) pore-size distributions as determined by NLDFT method of TPT, Fe_2O_3@TPT and Pd-Fe_3O_4@TPT, respectively.

The wide-angle powder XRD of the as-synthesized TPT based POP material was displayed in Figure S1. The two distinct broad peaks at 25° and 44° correspond to the π-stacking of the aromatic building blocks in small domains and the formation of the amorphous structure, which is composed of randomly polymerized TPA units. These peaks could be also nicely indexed by the diffraction planes of the carbon (002) & (101), respectively.[37] The PXRD patterns of Fe_2O_3@TPTand Pd-Fe_3O_4@TPT are shown in Figure 2b, which clearly depicts the rhombohedral structure of α-Fe_2O_3 with the characteristic Bragg's diffraction peaks at 2θ = 24.1°, 30.1°, 35.5°, 40.8°, 49.3°, 53.9°, 57.5°, 62.3° & 64.0°, corresponding to the (012), (104), (110), (113), (024), (116), (214), (300) diffraction planes, respectively.[38] For the Pd-Fe_3O_4@TPT nano-hybrid, distinct peaks of Pd nanoparticles at 40.18°, 46.76° and 68.16° are indexed as Pd(111), Pd(200) and Pd(220), respectively. The inverse spinel structure of magnetite

is confirmed by the assigned (220), (311), (400), (422), (511), (440) reflections.[39] Interestingly, the synthesis of Fe_2O_3@TPTand Pd-Fe_3O_4@TPTnano-catalyst were performed in the same reaction condition, despite having ended up with two different phase of iron oxides. We note that, the Pd NPs played the crucial role for the formation of magnetite (Fe_3O_4), which are generated through *in situ* reduction, facilitated by PVP from the metal precursor. Pal *et al.* described the redox properties of Pd NPs and indicated that the relatively small Pd NPs can act as effective reducing agents.[40] Recently, the promoted reduction of hematite to magnetite by Pd NPs was reported by Espro*et al.*[41] The surface morphology is explored through FE-SEM analysis, which clearly indicates the formation of highly rough surface of TPT-POP (Figure S3). Random aggregation of particles, formed during the high temperature synthesis, lead to the observation of chunks on the TPT-POP surface. FE-SEM images of Fe_2O_3@TPT and Pd-Fe_3O_4@TPT(Figure S5 & S6) reveal the pearl millet like morphology, making the surface rough in texture. By evaluating the lower magnification FE-SEM images, we can clearly observe parched earth-type morphology, indicating the formation of iron oxide-wrapped porous organic polymer. The average size of the conjugated spherical Fe_2O_3@TPT and Pd-Fe_3O_4@TPT particles appears to be in the range of 21-65 nm and 7-25nm, respectively. Energy dispersive X-ray (EDX) analysis (Figure S7) of the selected areas of the FE-SEM micrographs clearly signifies the presence of N, O, Fe and Pd in the respective spectra. In order to further investigate the surface morphology and the electronic properties, TEM analysis was performed (Figure 3). Close inspection of the TEM image of the parent TPT-POP (Figure S4) reveals cloud-like surface morphology, resulting in a hyper-branched porous nature. At 50 nm scale, spider web-type morphology was noticed, probably owing to the hyper-cross-linking between two monomers, along with the irregular dispersion of metal nanoparticles over the porous network. The two different phases of iron oxide (Fe_2O_3, Fe_3O_4) and Pd nanoparticles are distributed randomly over the fibrous polymer network, as shown in Figure 3a &3e. In figure 3f, dark regions represent the presence of Pd nanoparticles, whereas Fe_3O_4 particles are intertwined with the relatively brighter polymeric network of Pd-Fe_3O_4@TPT (). HR-TEM images of Fe_2O_3@TPT and Pd-Fe_3O_4@TPT nanoclustures show lattice fringes of the Fe_2O_3 (104) & Fe_2O_3 (012) and Fe_3O_4 (311) & Pd (111), respectively crystal planes , consistent with the PXRD data. The selected area electron diffraction (SAED) patterns reveal d-spacings that correspond to lattice fringes of rhombohedral α-Fe_2O_3 and spinel Fe_3O_4 & Pd metal, as shown in Figure 3d & 3h, respectively; this observation

is also in good agreement with the JCPDS nos. (33-0664), (19-0629), and (46-1043). STEM micrographs (Figure 3i & j) of Fe_2O_3@TPT & Pd-Fe_3O_4@TPT depict comparably large stationary metal phases distributed randomly amongst the somewhat extensive agglomeration of nanoparticles.

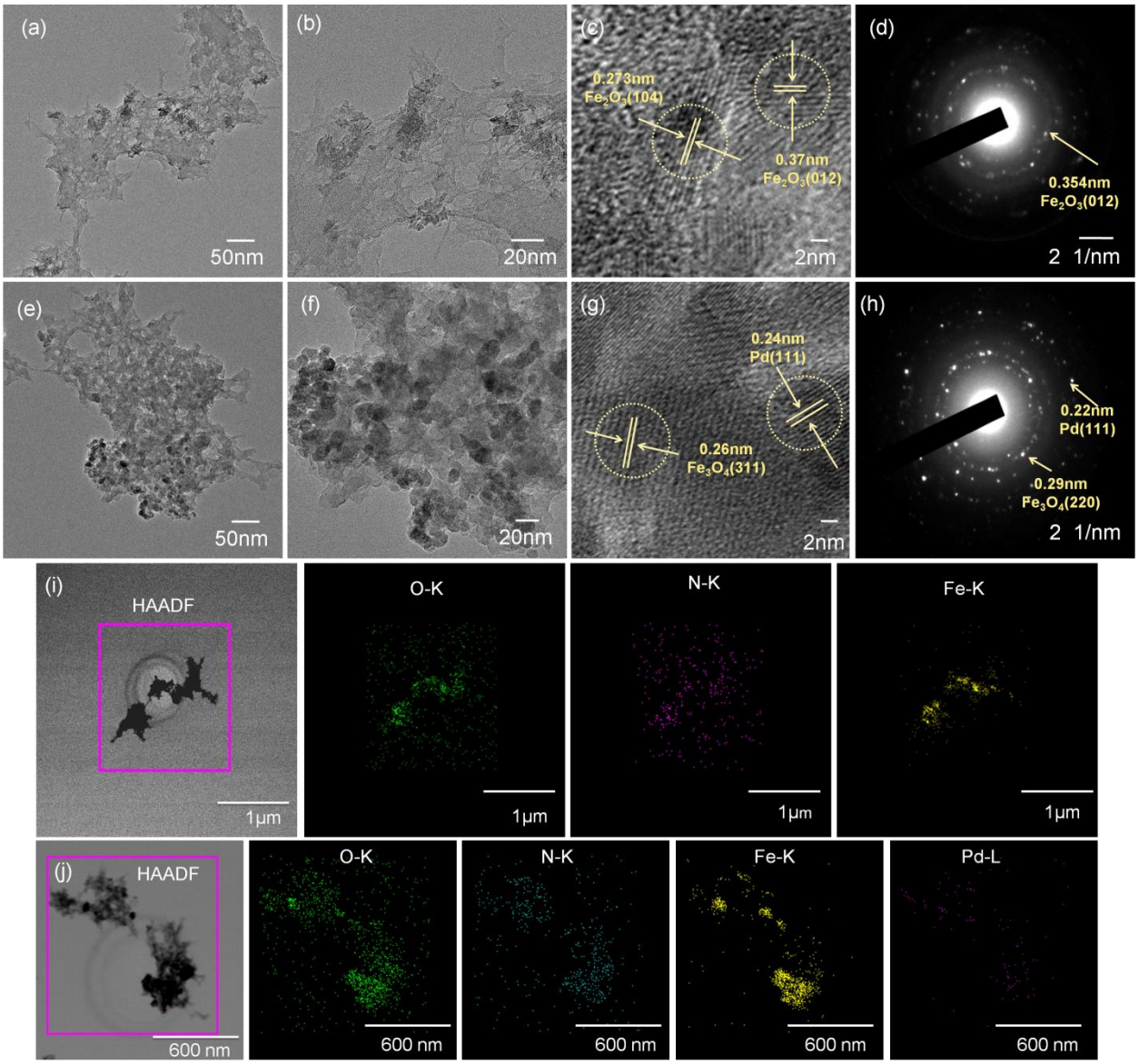

Figure 3: TEM images of Fe_2O_3@TPT (a & b) and Pd-Fe_3O_4@TPT (e & f). HR-TEM images with clear crystalline lattice fringes of Fe_2O_3@TPT (c) & Pd-Fe_3O_4@TPT (g). SAED (selected area electron diffraction) patterns were also provided for Fe_2O_3@TPT (d) and Pd-Fe_3O_4@TPT (h); STEM images of Fe_2O_3@TPT (i) and Pd-Fe_3O_4@TPT (j) with the corresponding elemental mapping of O, N, Fe and Pd.

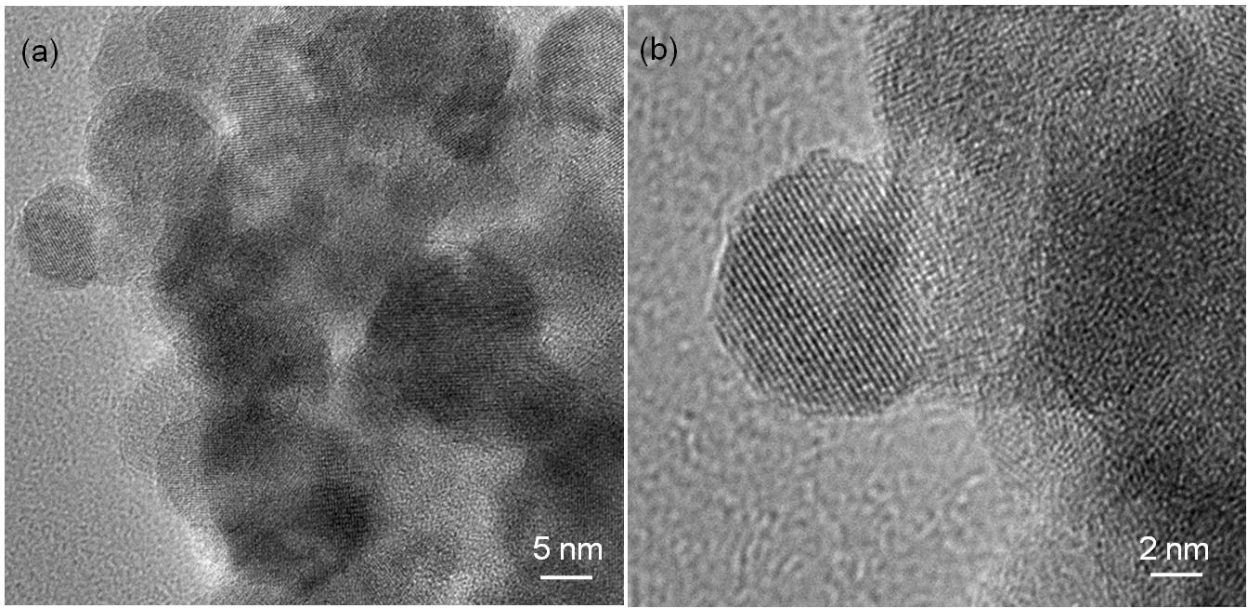

Figure 4: High-resolution TEM images at different magnifications of Pd-Fe_3O_4@TPT.

Additionally, elemental mapping of both integrated catalysts reveals that each of the O, N, Fe, and Pd elements is locally concentrated at specific regions. The representative high resolution TEM image (Figure 4a) depicts considerably rough spherical particles Fe_3O_4 of 9.97-12.42 nm in diameter, which can be spotted on the exterior surface of the TPT-POP after Pd-mediated reduction. Moreover, the TEM image of the near-surface region (Figure 4b) demonstrates two phases of Fe_3O_4 with different electron densities, owing to the high surface energy compared to that of TPT-POP with low roughness.

X-ray photoelectron spectroscopy (XPS) was analyzed to shed light on the elemental composition and oxidation state of each element on the surface of Fe_2O_3@TPT and the Pd-Fe_3O_4@TPT nano-hybrid. The characteristic peaks of N, O, Fe and Pd in the as-synthesized porous material was indicated by the XPS survey spectra (Figure S9). The highest binding energy peak at ~399.6 eV (Figure S8b & S8d) in the N 1s spectrum corresponds to the N-atom connected to the benzene ring of triphenyl amine monomer (C=C-N) for both nano-composites.[42] In the O 1s spectrum, binding energy peaks appear at ~530eV and ~531.66 eV (Figure S8a, Figure S8c), which can be attributed to the lattice oxygen (Fe-O) and the hydroxyl group on the polymers' surface.[43-45] The presence of α-Fe_2O_3 phase in Fe_2O_3@TPT was confirmed by the binding energy peaks at ~711.83 eV and ~725.51 eV (Figure 5a), which correspond to Fe $2p_{3/2}$ and Fe $2p_{1/2}$, respectively, along with a shake-up satellite peak at ~719.74 eV.[46] A slight positive shift in binding energy relative to bare Fe_2O_3 is noticed; this is in good

agreement with the literature,[43] attributed to the interaction of Fe^{+3} with the hydroxyl groups the N atoms in the polymeric framework. For Pd-Fe_3O_4@TPT, the characteristic binding energy peaks at ~711.92 eV and ~725.67 eV (Figure 5b) reveal the presence of magnetite.[43] Binding energy peaks indexed at ~336.19 eV and ~341.18 eV (Figure 5c) in the XPS spectra corresponds to the Pd $3d_{5/2}$ and Pd $3d_{3/2}$ orbitals, respectively, of metallic Pd^0 in Pd-Fe_3O_4@TPT. However, comparing the XPS data of Pd-Fe_3O_4@TPT with bare Pd-NP, the negative shift of around ~0.3 eV signifies the electron enrichment of Pd^0 due to the interaction between N-atom and the Pd-NPs in Pd-Fe_3O_4@TPT.[47]

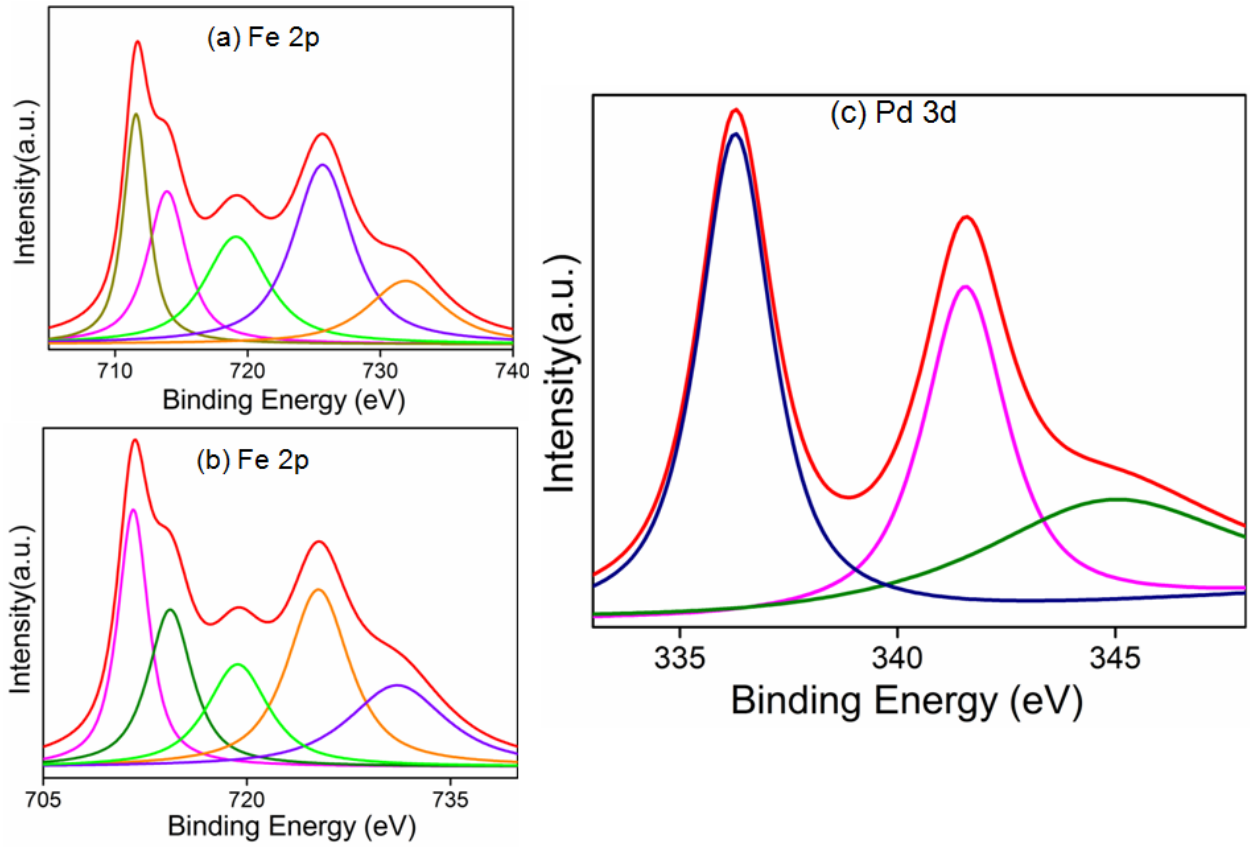

Figure 5: XPS spectra of Fe-2p for Fe_2O_3@TPT(a)& Pd-Fe_3O_4@TPT (b); Pd-3d spectrum for Pd-Fe_3O_4@TPT (c).

To unfold the reason behind the superior catalytic activity of Pd-Fe_3O_4@TPT, detailed information, including local structure, oxidation state of each element, and Fe, Pd density were extracted from X-ray absorption near edge structure analysis (XANES). The Pd K-edge XANES/EXAFS spectra of the Pd-Fe_3O_4@TPT sample look similar to those of Pd foil, indicating that most Pd atoms are present in metallic state and aggregated to form Pd clusters.[47]

However, the Pd-Pd coordination number of the Pd-Fe_3O_4@TPT sample is 10.2, significantly smaller than 12 for Pd foil with a bulk *fcc* structure (as reflected by the reduced EXAFS intensity both in k-space and in R-space). The Pd-Pd coordination number of 10.2 corresponds to an average Pd cluster size of roughly 3 nm. The Pd-Pd and Fe-Pd coordination in the first coordination sphere is represented by the peak at around ~2.49 Å (Figure 6b).[48] Comparing with the typical Pd-Pd bond distance of around ~2.7 Å, the observed value of 2.49 Å signifies the formation of Pd-Fe bonds in the Pd-Fe_3O_4@TPT sample.[50] As the radius of Fe atom (1.27 Å) is small compare to the radius of Pd atom (1.38 Å), the overall lattice constant is reduced and is responsible to the observed interatomic distance.[48,49] The deviation in Fe-Pd bond from the theoretical value of 2.6 Å may be due to the interaction between Pd NPs, Fe_3O_4 and the TPT-POP material. The Fe K-edge spectra of the Fe_2O_3@TPT sample are very similar to those of standard alpha-Fe_2O_3. However, the Fe-O bond length of 1.92 Å of the Fe_2O_3@TPT sample is slightly longer than that the 1.89Å of the Fe_2O_3 standard, probably resulting from interactions between Fe_2O_3 and TPT-POP. Such interactions caused the Fe_2O_3 lattice to expand to some extent. Both XANES and EXAFS spectra of the Fe K-edge of the Pd-Fe_3O_4@TPT sample are similar to those of standard Fe_3O_4. At a closer examination, either the white-line peak or the pre-edge peak of the Pd-Fe_3O_4@TPT sample shifted to a lower energy relative to the standard Fe_3O_4 (but still higher than those of the standard FeO). It seems that the overall spectral features were contributed by both Fe_3O_4 and FeO phases (with the former being in majority). The Fourier transform of the EXAFS (FT-EXAFS) spectrum of Pd-Fe_3O_4@TPT exhibits a strong peak between 1.0-2.0 Å in R-space, which also supports the above speculation. Another strong peak between 2.5-3.5 Å represents the Fe-Fe shell, which is confirmed by the reference Fe_3O_4 spectrum.[51] On the whole, this XAS observations indicate that the Fe species in Pd-Fe_3O_4@TPT is similar in nature to Fe_3O_4. Here, Pd NPs play a vital role in the preparation of Pd-Fe_3O_4@TPT, as it promotes the reduction of $Fe_2O_3$to Fe_3O_4.

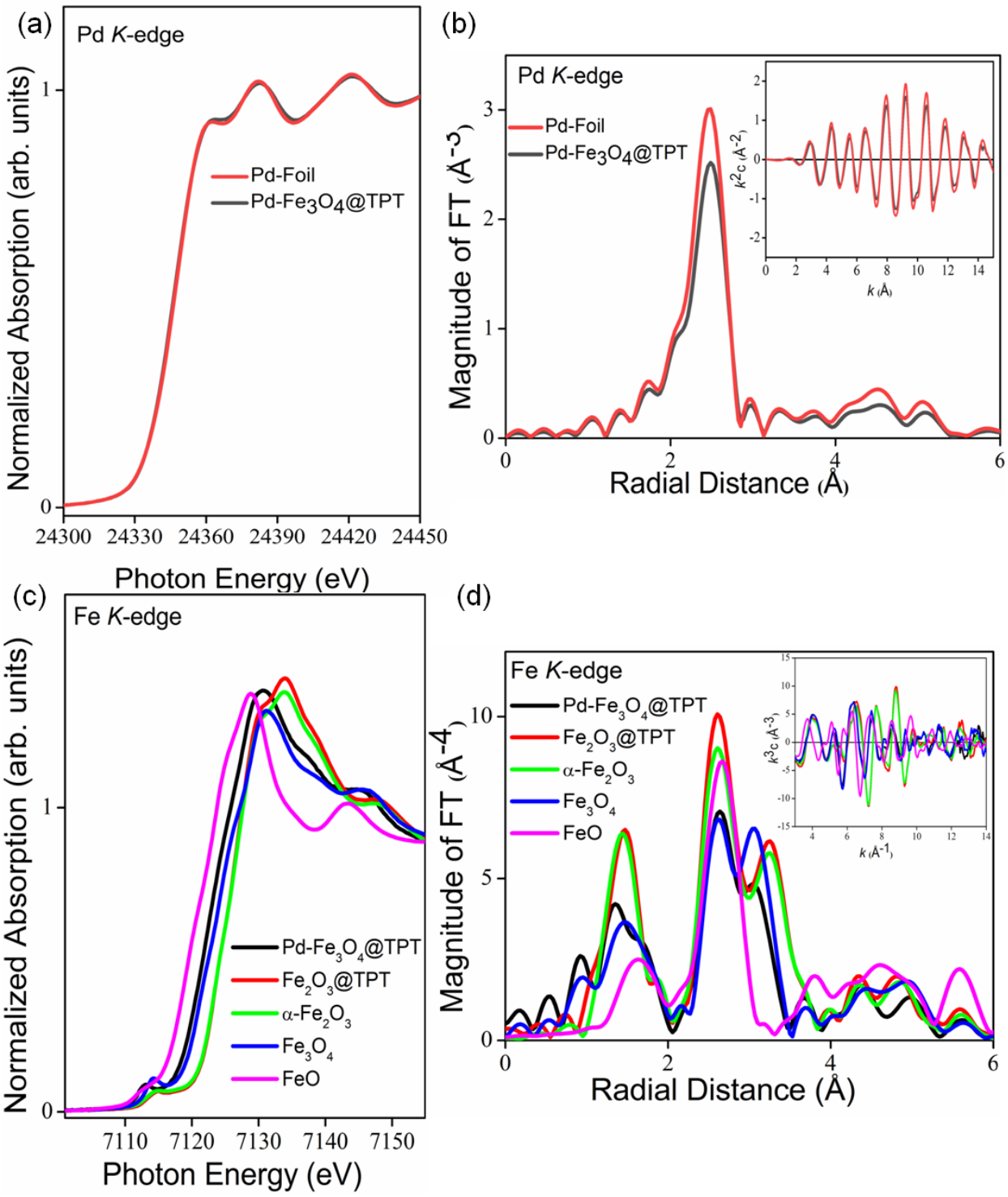

Figure 6: The normalized XANES spectra (a) and k_2-weighted Fourier transform EXAFS spectra (b) at the PdK-edge of Pd-Fe_3O_4@TPT and bulk Pd foil. The normalized XANES spectra (c) and k_3-weighted Fourier transform EXAFS spectra (d) of the samples (Pd-Fe_3O_4@TPT and Fe_2O_3@TPT) and the relative standards (α-Fe_2O_3, Fe_3O_4 and FeO) at the Fe K-edge.

Selective Hydrogenation of Cinnamaldehyde over Pd-Fe_3O_4@TPT and Fe_2O_3@TPT:

Selective hydrogenation of α, β-unsaturated aldehyde is crucial for the production of useful intermediates in the pharmaceutical, cosmetics and food industries. Here, cinnamaldehyde was selected as a model compound, which consists of distinct types of unsaturated functional groups, such as C=C and C=O, along with the extended conjugation with the benzene ring. Selective hydrogenation of cinnnamaldehyde gives rise to different types of unsaturated aldehyde and alcohol, *i.e*. double bond reduction leads to the formation of hydrocinnamaldehyde (HCAL) whereas C=O reduction produces cinnamylalcohol (COL). Initial reaction study was carried out for the selective hydrogenation of cinnamaldehyde (2 mmol, 0.25 ml) in 30 ml isopropanol over Pd-Fe_3O_4@TPT (30 mg) and 10 bar H_2 at 60 °C for 1h with constant stirring. The comparison study was performed under identical conditions to optimize the reaction temperature, pressure and time. At the end of each reaction, the products obtained were analyzed by GC-FID. The progress of the catalytic hydrogenation of cinnamaldehyde over Pd-Fe_3O_4@TPT as a function of time at 60 °C and 80 °C are shown on Figure 7a and Figure 7b, respectively. After the initial 0.5 h of reaction at 60 °C and 10 bar pressure, 94% conversion of cinnamaldehyde, accompanied by 100% selectivity towards hydrocinnamaldehyde, was observed. Complete conversion of cinnamaldehyde along with 100% hydrocinnamaldehyde selectivity was obtained with 1 h advancement of the reaction, although further increment in reaction time facilitates the production of phenyl propanol as the byproduct from hydrocinnamaldehyde. Time on stream profile at 80 °C reveals no further conversion of cinnamaldehyde after the initial 0.5 h. The same trend of increasing conversion and selectivity with time is also noticed at 80 °C. The full conversion of cinnamaldehyde was attained after 1h, followed by 82% and 18% selectivities towards hydrocinnamaldehyde and phenyl propanol, respectively. The prolongation of reaction time to 3 h decreased the selectivity of hydrocinnamaldehyde to 73% while increased the byproduct selectivity to 27%.

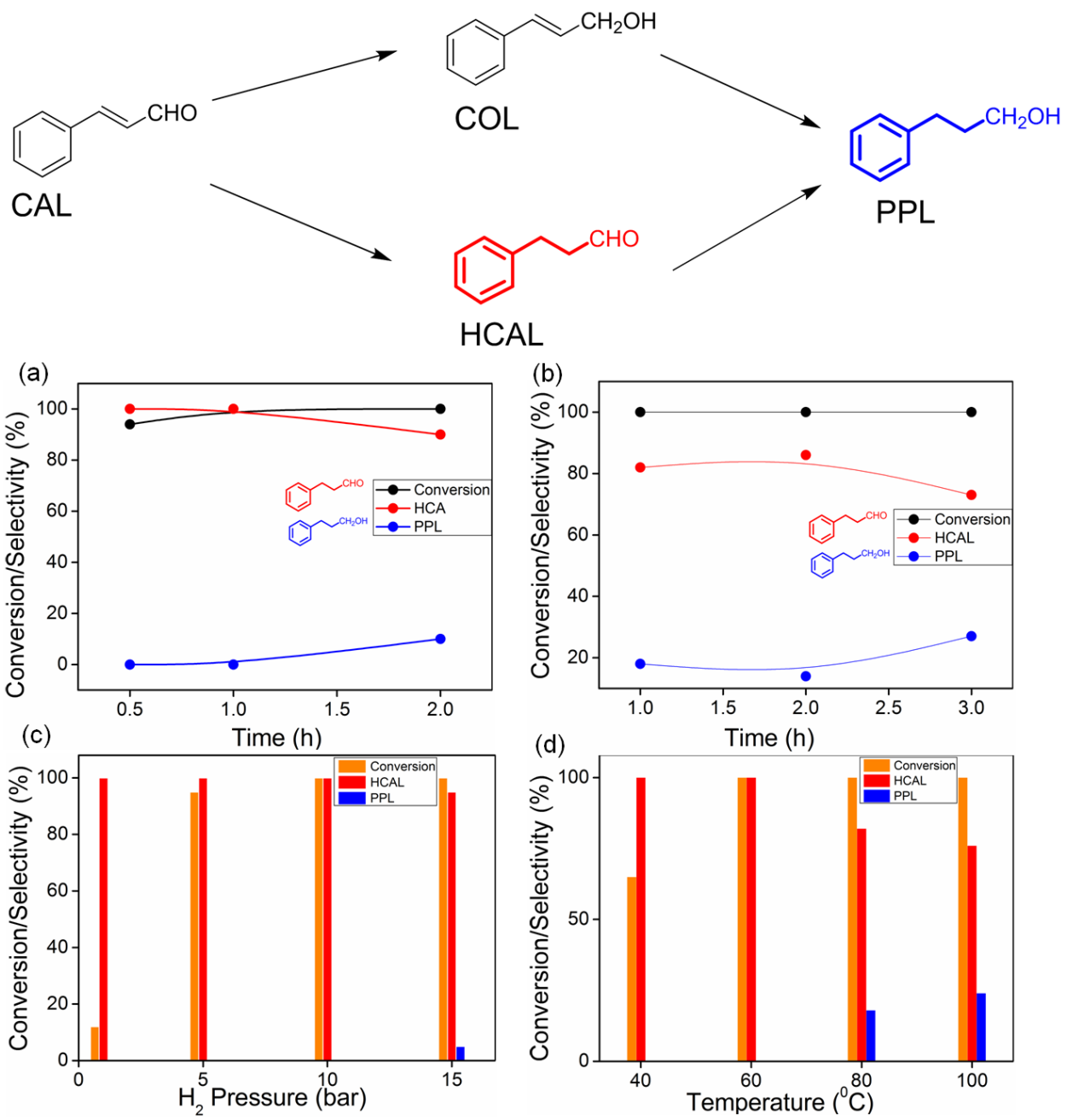

Figure 7: Evolution of reactant and product distributions against time for selective hydrogenation of cinnamaldehyde at two different temperature of 60 °C (a) and 80 °C (b); Effect of H_2 pressure (c) and Influence of reaction temperature (d) over the Pd-Fe_3O_4@TPT catalyst. Reaction conditions: Cinnamaldehyde (0.25ml, 2 mmol), Pd-Fe_3O_4@TPT (30 mg), 60 °C, 1 h in 30 ml of isopropanol; the other product refers to phenyl propanol.

A series of reactions were also carried out at different H_2 pressures to evaluate the optimum pressure for the reaction at 60 °C with 1 h reaction time (Figure 7c). Interestingly, 12% conversion of cinnamaldehyde and 100% selectivity towards hydrocinnamaldehyde was

achieved at 1 bar H_2 pressure. At 5 bar, the conversion of CAL and selectivity of HCAL increased to 95% and 100%, respectively. Finally, the full conversion of cinnamaldehyde with 100% hydrocinnamaldehyde selectivity was secured at 10 bar H_2 pressure. Although the full conversion of cinnamaldehyde occurred at 15 bar H_2 pressure, the selectivity of hydrocinnamaldehyde degraded to 95% with a byproduct selectivity of 5%. The progress of the cinnamaldehyde hydrogenation as a function of temperature was provided in Figure 7d for Pd-Fe_3O_4@TPT. The initial 65% conversion of cinnamaldehyde, accompanied by 100% hydocinnamaldehyde selectivity was observed at 40 °C, after 1 h of reaction. At 60 °C and 10 bar pressure, complete conversion of cinnamaldehyde to hydrocinnamaldehyde was detected in 1 h. When the temperature was raised to 80°C, hydrocinnamaldehyde selectivity lowered to 82%, owing to the further conversion to other byproducts (18%) at higher temperatures. The trend of increasing selectivity towards other byproduct remains unaltered even at 100 °C, giving rise to 24% selectivity towards phenyl propanol. We have also conducted the catalytic reaction at room temperature 25 ºC (Table 1, entry 9). In this case, we have achieved 40% conversion of cinnamaldehyde with 100% selectivity of hydrocinnamaldehyde under optimized reaction conditions.

To shed light on the key factors contributing to the enhanced catalytic activity of the Pd-Fe_3O_4@TPT catalyst, we investigated the interaction of cinnamaldehyde with the surface of the catalyst by ATR-IR spectroscopy. Horiuti-Polayni mechanism suggests that the hydrogenation of α, β- unsaturated aldehyde involves three different adsorbed states, correspondingly di-σC = Oη^2, di-σC = Cη^2 and di-πη^2(η^4). [52-55]. Also, the metal d-band center plays a crucial role in determining the product selectivity during the hydrogenation of α, β- unsaturated carbonyl compounds.[56] From Huckel calculations, it has already been established that the interaction between the metal surface and the conjugated C=C bond increases relative to that with the C=O bond with decreasing energy level of the metal d-band center, which is in the order: Pd < Pt < Ir ≈ Os.[57,58] Selectivity of the interaction between metals and C=C bond has been established by DFT calculations[59] and HREELS study[60], which showed that maleic anhydride interacts through C=C bond with Pd (111) instead of C=O bond. These factors suggest that the C=C bond of CAL has more affinity towards hydrogenation by Pd metal-activated H_2 than the C=O bond.

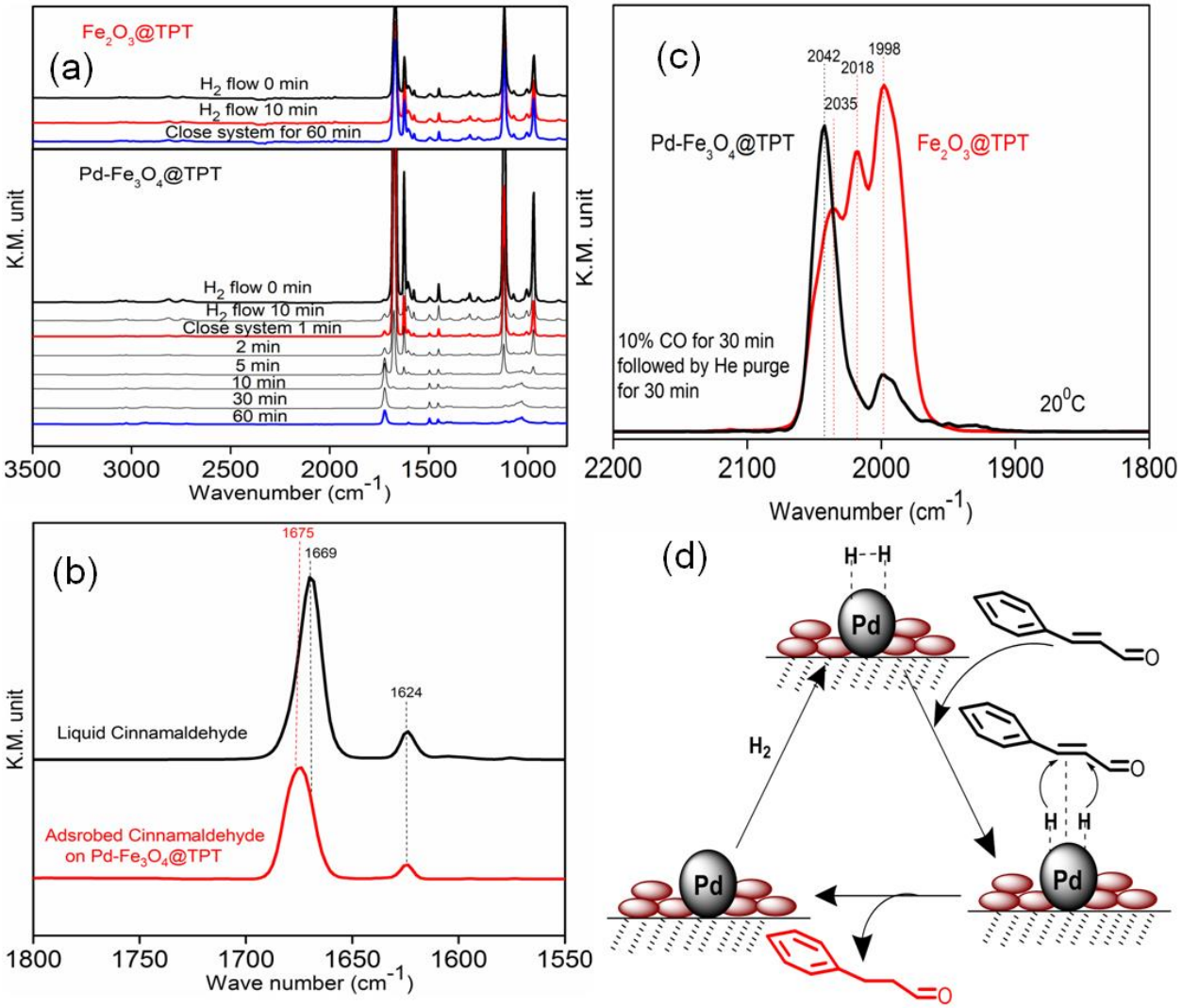

Figure 8: (a) *In situ* ATR spectra of CAL hydrogenation on Fe_2O_3@TPT and Pd-Fe_3O_4@TPT, (b) DRIFTS spectra of CAL adsorption on Pd-Fe_3O_4@TPT sample after drop of CAL at 60 ^oC and subsequently flushing with He for 60 min at 250 ^oC, (c) DRIFTS spectra of CO adsorption on Fe_2O_3@TPT and Pd-Fe_3O_4@TPT, (d) Plausible mechanistic pathway for the selective hydrogenation of CAL to HCAL. **Reaction conditions**: Cinnamaldehyde (0.25 ml, 2 mmol), Pd-Fe_3O_4@TPT (30 mg), solvent (30 mL), 10 bar H_2 pressure, 60°C; Time (1 h).

From the ATR analysis, characteristic peaks of liquid phase CAL on Pd-Fe_3O_4@TPT are shown in Figure 8a. Flowing hydrogen over Pd-Fe_3O_4@TPT led to the appearance of a peak at 1722 cm^{-1}, which could be attributed to the C=O vibration of hydrocinnamaldehyde.[61] Further reaction in a sealed H_2 atmosphere resulted in an increase in the intensities of this peak, accompanied by a

gradual disappearance of all the characteristic peaks of CAL. In contrast, the IR spectra of CAL hydrogenation over Fe_2O_3@TPT remained unchanged, manifesting the essential role of Pd in activating H_2. The observations by *in situ* ATR reflected a clear reaction pathway, *i.e.* the preferential hydrogenation of the C=C bond over the C=O bond over Pd-Fe_3O_4@TPT. Initially, CAL molecule is adsorbed on the Pd metal surface through the C=C bond. Simultaneously, H_2 molecules dissociatively adsorb onto the electronically promoted Pd NPs. Then, activated hydrogen species attaches the adsorbed C=C bond of the, followed by desorption of the HCAL product. Accordingly, Figure 8d presents the mechanistic pathway of selective hydrogenation of CAL to HCAL over Pd-Fe_3O_4@TPT. On the other hand, the presence of mesoporous channel on the as-synthesized catalyst facilitated the rapid removal of hydrocinnamaldehyde from the active sites, thus preventing the further hydrogenation of HCAL to PPL.[13] The CAL adsorption DRIFTS spectra in Figure 8b shows an obvious blue shift of peaks assigned to the vibrations of C=O bonds, from 1669 cm^{-1} to 1675cm^{-1} over the Pd-Fe_3O_4@TPT, which suggests that the adsorption CAL on the surface of Pd-Fe_3O_4@TPT resulting a shortening of the C=O bond.[62-64] Therefore, the hydrogenation of C=O was hindered. In contrast, the peak at 1624 cm^{-1}, assigned to the C=C bonds, remained almost unchanged compared to the liquid phase standard. Figure 8c reveals three DRFIT CO adsorption peaks over the Fe_2O_3@TPT sample, which could be attributed to the CO adsorption on Fe of different valences.[65] Nonetheless, a sharp peak at 2042 cm^{-1} is observed over the Pd-Fe_3O_4@TPT catalyst; this peak is ascribed to the ontop CO adsorbed on Pd.[66]

We have also screened the use of various solvents with hydrogen-bond-acceptance ability (HBA), whilst fixing the temperature at 60 °C. The progress of the catalytic reaction with CAL conversion, along with the various products selectivity, are presented in Table S2. Isopropanol was found to be the best solvent among all the solvents screened. However, the selectivity of HCAL decreased and whilst that of PPL increased when MeOH was the solvent. However, high selectivity toward HCAL was obtained in water, despite the low conversion of CAL after 1 h.

We subsequently conducted the chemoselective hydrogenation of cinnamaldehyde using different catalysts, as listed in Table 1. We could observe that, in the absence of any catalytic active metal sites, bare TPT appears to be completely inactive (Entry 1, Table 1). When the reactions were conducted with monometallic Pd or Fe_3O_4-NPs, poor catalytic activities have also been encountered (Entry 2 & 3, Table 1). When the Pd-Fe_3O_4 NPs were mechanically mixed

with TPT-POP, it displayed an almost similar CAL conversion to that of unsupported Pd NPs, but despite a slight improvement (38%) (Entry 5, Table 1). The promoted performance could be attributed to the presence of the Pd-Fe_3O_4 interface, which modulates the electronic property of metal sites, effectively enhancing the catalytic activity. However, no further improvement in the conversion of CAL was noticed for the Pd@TPT catalyst, which preferred the over hydrogenation product of 1-phenyl propanol (PPL) (Entry 7, Table 1). When the Fe_3O_4 was deposited on the TPT-POP support (Fe_3O_4@TPT), both the conversion and selectivity for the catalyst were low (Entry 6, Table 1). Xiao *et al.* also reported the inertness of bare Fe_3O_4 & Fe_3O_4@C towards the hydrogenation of cinnamaldehyde, in strong agreement with our findings of Fe_3O_4@TPT.[69] Moreover, the dissociative activation of H_2 on Fe_3O_4 was sluggish compared to that on Pd-Fe_3O_4, resulting in the poor catalytic activity of Fe_3O_4@TPT. In contrast, electronically enriched Pd NPs interact with the Fe oxide species, which promotes the splitting of H_2 molecule to form non-polar H atoms over the Pd surface, thereby accelerating the catalytic conversion. In a control experiment, we synthesized a Ni-Fe_3O_4@TPT catalyst, which achieved low cinnamaldehyde conversion (~5%) under optimized reaction conditions (Table 1, entry 8); this observation further highlight the importance of the Pd-Fe_3O_4 interface. Based on our systematic investigation, we can confidently conclude that the combination of TPT-POP support with the Pd-Fe_3O_4 interface plays a decisive role in promoting the catalytic activity.

Table 1: Catalytic activity of various catalysts for chemoselective Hydrogenation of Cinnamaldehdye (CAL)

Entry	**Catalyst Used**	**Con of CAL (%)**	**Sel of HCAL (%)**	**Selectivity of PPL (%)**	**Selectivity of COL (%)**
1	TPT	0	0	0	0
2	Pd-NPs	26	20	6	0
3	Fe_3O_4-NPs	15	10	2	3

4	Pd-Fe_3O_4@TPT	100	100	0	0
5	Pd-Fe_3O_4@TPT (Physical Mixture)	38	36	2	0
6	Fe_3O_4@TPT	10	10	0	0
7	Pd@TPT	72	65	7	0
8	Ni-Fe_3O_4@TPT	5	100	0	0
9*	Pd-Fe_3O_4@TPT	40	100	0	0

Reaction conditions: Cinnamaldehyde (0.25 ml, 2 mmol), Catalyst (30 mg), isopropanol solvent (30 mL), 10 bar H_2 pressure, 60 °C; Time (1 h). *Reaction was carried out at room temperature (25 ºC).

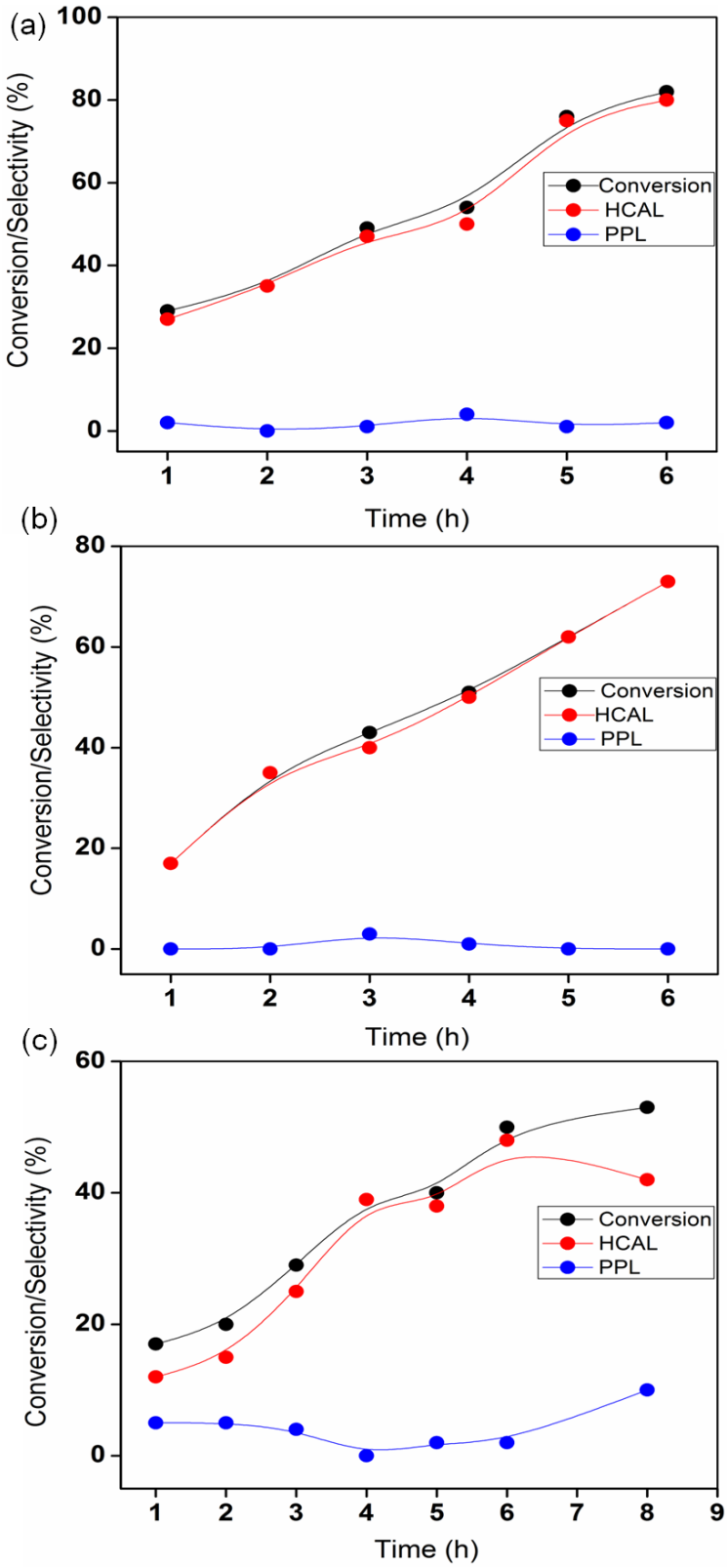
(a)
Conversion/Selectivity (%)
Time (h)
Conversion
HCAL
PPL
(b)
Conversion/Selectivity (%)
Time (h)
Conversion
HCAL
PPL
(c)
Conversion/Selectivity (%)
Time (h)
Conversion
HCAL
PPL

Figure 9: Evolution of reactant and product distribution against time of different supports Pd-Fe_3O_4@SiO_2(a), Pd-Fe_3O_4@C (b), bare Pd-Fe_3O_4-NPs(c), respectively. Reaction Conditions: Cinnamaldehyde (0.25ml, 2 mmol), 60°C, 30 ml of isopropanol.

To demonstrate the importance of the TPT-POP support, a comparative study was performed using other synthetic catalysts including Pd-Fe_3O_4@SiO_2 and Pd-Fe_3O_4@C. All catalysts were prepared following similar synthesis procedures. The evolutions of reactant and product distributions over time for the three catalysts tested are plotted Figure 9. It can be clearly observed that the CAL to HCAL conversion become sluggish in comparison to the Pd-Fe_3O_4@TPT-POP catalyst. The high catalytic activity of Pd-Fe_3O_4@TPT and Pd-Fe_3O_4@SiO_2 compared to the Pd-Fe_3O_4@C could be attributed to the presence of surface -OH groups, which binds strongly to the hydrophilic COL, thereby hindering its desorption and promoting the selectivity towards HCAL. The presence of porous channels leads to the faster diffusion of CAL and enables the easy access of the reactants to the active Pd sites to furnish the desired products. We also note that Pd-Fe_3O_4@TPT appears to be far more active than Pd-Fe_3O_4@SiO_2. Xiao *et.al* have developed a magnetically responsive core-shell Pd/Fe_3O_4@C composite catalyst for the hydrogenation of cinnamaldehyde. Their Pd/Fe_3O_4@C catalyst achieved 70% selectivity to hydrocinnamaldehyde under 14 bar pressure at 80 °C after 10 h reaction time.[71] In comparison, Pd-Fe_3O_4@TPT-POP attained hydrocinnamaldehyde with 100% selectivity at 60 ºC after only 1 h reaction time, demonstrating the superiority of our catalyst design strategy. Based on the results discussed above, we can rationalize that, the π-π interactions between the aromatic organic substrate and support matrix, as well as the large surface area favoring the hydrogenation of the intermediate to the desired product with fast and easy diffusion, facilitates the efficient chemical conversion.[70]

To verify the function of TPT-POP in promoting the selectivity during the Pd-catalyzed cinnamaldehyde hydrogenation, we performed Density Functional Theory (DFT) calculations to computationally examine the interaction between a monomer of the POP, triphenylamine (TPA), with the Pd cluster. All first-principle calculations were performed using periodic boundary conditions and plane-wave pseudopotential implemented in the Vienna ab-initio simulation package (VASP), developed at the FakultätfürPhysik of the Universität Wien. [72,73] Details of the calculations are described in the Supporting Information. We chose the optB88-vdW functional developed by Klimeš*et al.*[74,77] for the DFT calculations since it was reported to be the best level

of theory describing correctly the interaction between aromatic compounds with the surface of transition metals.[78,81] The model of Pd_{332} cluster was used to represent the Pd NP with a size of 3 nm,[82,80] which was consistent with the average Pd cluster size of *ca*. 3 nm, estimated based on a Pd-Pd coordination number of 10.2, obtained by fitting the Pd *K*-edge XAS spectra of the Pd-Fe_3O_4@TPT sample, as shown in Figure 6.

According to DFT calculations, three different binding configurations of TPA monomer with the Pd_{332} cluster are shown in Figure 10. The adsorption of TPA molecule on the flat terrace sites via the coordination of only one aromatic ring (Fig. 10a) has an strong adsorption energy of -189 kJ/mol; this value is in good agreement with earlier experimental and theoretical results reported in the literature for the adsorption on benzene on Pd(111) surface and demonstrates the very strong interaction between aromatic compound with transition metal surfaces.[79,83] When the adsorption occurs by the coordination of two aromatic rings of TPA at the step edge (Fig. 9b), the binding energies become significantly stronger by ~75 kJ/mol. The computed adsorption energy attains a maximum at 301 kJ/mol when two aromatic rings of TPA interact with Pd cluster at the corner site (Fig. 9c). The strong interaction of Pd cluster with the TPA compound at the step-edge and corner binding modes could be a factor leading to the high density of step sites on the fabricated Pd NPs. Due to the tilted structure of the TPA monomer (three aromatic rings are not planar and form corrugated structure around N atom) and the very strong binding to the Pd facets, the as-synthesized Pd NPs could be nucleated and grown along those corrugated sites between the tilted phenyl rings and finally form NP structures with high density of step sites. Consequently, the presence of the step sites could be an important factor contributing to the high selectivity of the Pd-Fe_3O_4@TPTto the cinnamaldehyde hydrogenation.

Indeed, the enhancement in the selectivity towards C=C hydrogenation in cinamaldehyde and in α, β-unsaturated aldehydes on steps sites and lower coordinated sites has been reported in literature.[84-86] While the hydrogenation of C=O bond is structure-insensitive, the hydrogenation of C=C bond was reported to be structure-dependent and promoted significantly at the step sites.[87,84] Serrano-Ruiz *et al*.[88] achieved a hydrocinnamaldehyde selectivity of 82% for cinamaldehyde hydrogenation on 3 nm Pt catalyst, which possesses high ratio of corner & edges atoms to terrace atoms. In contrast, 10 nm Pt catalysts with much lower density of step and edge sites gives a HCAL selectivity of only 49%. Zhang *et al*.[89] also reported great enhancement in the hydrogenation of cinamaldehyde towards hydrocinnamaldehyde on Pd cluster nanowire

catalyst with the enrichment of high index facets and step sites on the surface, whereas the activity and selectivity of cinamaldehyde hydrogenation on commercial Pd/C and Pd/γ-Al_2O_3 catalysts were more than one order of magnitude lower due to the lack of those active sites. Furthermore, in the hydrogenation of 3-methylcrotonaldehyde, the Pd(533) stepped surface was shown to be twice more active than the terrace Pd(111) plane in the study of Birchem et al.[90] Also in that study, when the step sites on Pd(533) stepped surface were blocked by a sub-monolayer of pre-adsorbed Sn, the selectivity towards the C=C bond hydrogenation was drastically reduced. The aforementioned studies emphasize the higher activity and selectivity of the step sites towards C=C bond hydrogenation to saturated aldehydes. Since the TPT polymer frame structure could act as the structural template for growing Pd NP with high density of step and corner sites, it could be responsible for the high HCAL selectivity during cinamaldehyde hydrogenation on our fabricated Pd-Fe_3O_4@TPT catalyst.

In addition to the structural factors discussed above, DFT calculations also revealed charge transfer between the TPA and the Pd_{332} cluster. From the Bader charge calculations, it is shown that there is a net transfer of 0.416 electron from the TPA monomer to the Pd_{332} cluster in their most stable interaction configuration, *i.e*. at corner site (Fig.10c). The charge transfer of electron from TPA to the Pd cluster induces the negative charge on the surface of the Pd cluster, which is also consistent with the observed negative shift of ~0.3 eV in the Pd $3d_{5/2}$ XPS spectra of Pd-Fe_3O_4@TPT (Fig.5c). As reported by recent studies, the C=C bond hydrogenation is very sensitive to the charge transfer. Accordingly, the charge transfer from the support to the metal cluster, imposing negative charges on the surface metal atoms, was found to dramatically increase the C=C bond hydrogenation activity.[91] This finding provides additional evidence that the modification of electronic properties induced by the TPT-POP promotes the selectivity towards hydrocinnamaldehyde formation during the cinamaldehyde hydrogenation on Pd-Fe_3O_4@TPT.

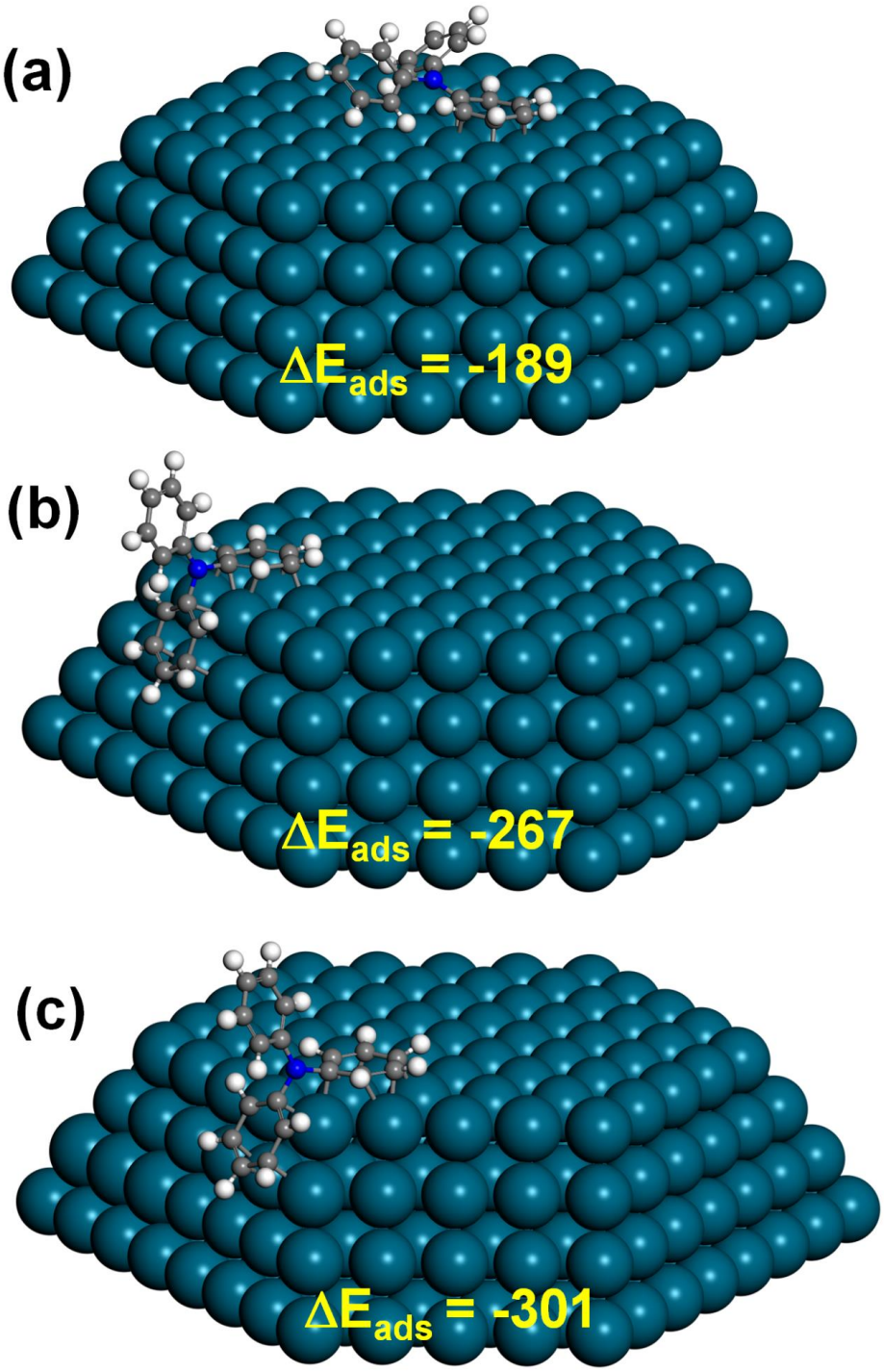

Figure 10: Different adsorption configurations of TPA molecule on the surface of a 3 nm Pd-NPs cluster: (a) adsorption on terrace sites. (b) adsorption at step sites. (c) adsorption at corner sites. Computed adsorption energies in kJ/mol are also indicated.

To perceive information about the durability and robustness of our Pd-Fe_3O_4@TPT catalyst, recyclability test was performed for 7^{th} consecutive catalytic cycles under optimized reaction

conditions. After each catalytic run, the catalyst was collected by washing with MeOH for 3 times and dried overnight at 80 °C; it was then used for the next cycle. As shown in Figure S11a, the catalytic conversion of CAL on Pd-Fe_3O_4@TPT catalyst slightly reduced between consecutive runs, although 100% selectivity towards the desired HCAL was maintained throughout the 7 cycles. The diminishment in catalytic activity over the seven cycles may be due to choking of the porous channel by the organic reactants or the rupture of surface exposed bimetallic nanoparticles caused by the inevitable intergranular friction, followed by collision with the stirrer and autoclave wall under the constant vigorous stirring conditions. We also conducted hot-filtration test to examine the leaching of metal species after quenching the reaction and the removal of the catalysts (See supporting information for details). It is quite evident from Figure S11b that, when the reaction initiated, the conversion quickly increased to about 76.3% in 15 minutes. However, no further CAL conversion was observed after separating the catalyst from the reaction mixture, manifesting the absence of Pd species in the reaction liquor. This result shows that Pd-Fe_3O_4 NPs was steadily hosted inside the porous organic nanocage in such a way that negligible leaching took place during the catalytic reaction. Furthermore, we conducted ICP-MS analysis of the recovered catalyst after each catalytic run (results shown in Table S3, SI). The ICP-MS results indicate the robustness feature of the catalyst, as the Pd and Fe contents in the recovered catalyst appeared to be similar to those in the fresh one. TEM images with SAED (selected area electron diffraction) patterns of the reused catalyst after the 2^{nd}, 4^{th} and 6^{th} catalytic runs were shown in Figure 11. From the Figure 11 a & b, it is quite evident that the density of the metal NPs their dimensions are comparable to the ones in the fresh catalysts. It is also apparent from Figure 11b that the NPs after 2 cycles are close to being spherical, highly crystalline nature (Figure 11c), with a mean sizes of about 18.8-22.8 nm. In contrast, we notice severe agglomeration of the NPs after the 4^{th} catalytic run, while the average particle sizes increased to about 25.8 nm (Figure 11e). Figure 11 f & i confirmed the diminishment of crystallinity of the NPs after the 6^{th} catalytic run, accompanied by the appearance of large particles with sizes up to 47.4 nm). This phenomenon could be explained by the surface aggregation of hydrophobic organic reactant, which leads to the blockage of active sites and the observed drop in HAL conversion.

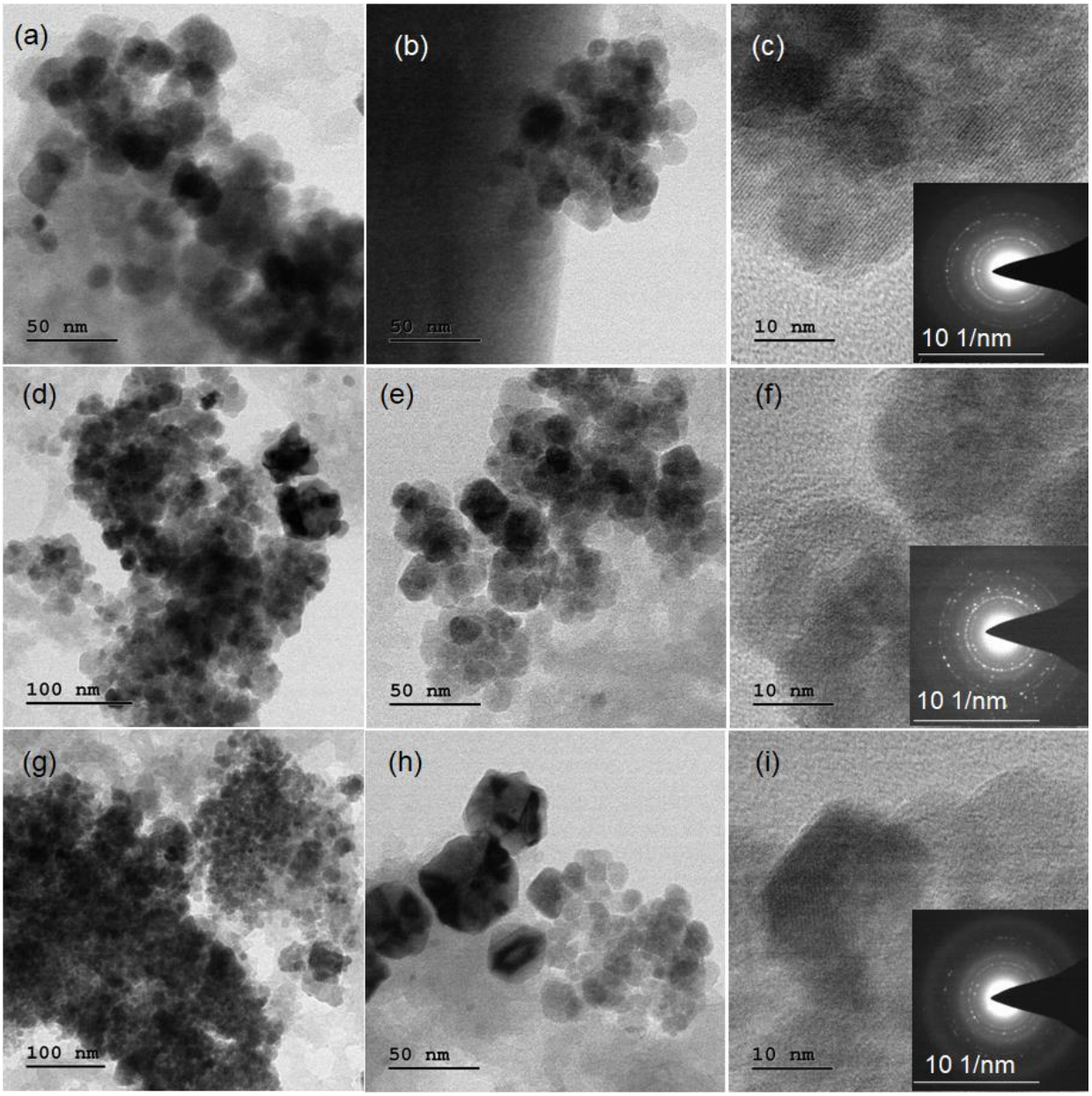

Figure 11: TEM images of the recycled Pd-Fe_3O_4@TPT catalyst after the 2^{nd} (a, b & c), 4^{th} (d, e & f) and 6^{th} (g, h &i) catalytic runs. SAED patterns have been provided in the inset of c, f & k, respectively.

Conclusions

In summary, we have successfully synthesized bi-functionalized TPT-POP *via* a simple metal & template-free condensation-polymerization route, utilizing triphenylamine and terephthaldehyde as the main building block and the cross-linker, respectively. Subsequently, we have implemented this synthesis strategy and prepared an integrated Pd-Fe_3O_4@TPT catalyst by an *in situ* encapsulation and reduction approach, in which Pd acts as a promoter for the reduction of Fe_2O_3 to Fe_3O_4. The as-synthesized TPT-POP and Pd-Fe_3O_4@TPT catalyst were comprehensively characterized by FTIR, solid-state ^{13}C CP-MAS NMR spectra, elemental analysis, EDX, PXRD, SEM, TEM, and physical adsorption-desorption of nitrogen at 77 K. The Pd-Fe_3O_4@TPT catalyst showed excellent activity for chemoselectivecinnamaldehyde (CAL) hydrogenation to hydrocinnamaldehyde (HCAL) under mild reaction conditions (P_{H2} = 10 bar, T = 60 ºC), whereas the Fe_2O_3@TPT catalyst was inherently inert. Moreover, Pd-Fe_3O_4@TPT retained excellent catalytic performance up to seven reaction cycles, demonstrating superior stability. Synchrotron EXAFS revealed structural changes at an atomic-scale, as manifested by the decrease in the Pd-Pd bond distance (~2.7 Å to ~2.49 Å), Fe-Pd bond formation, along with the shift of the Fe K-edge to a lower energy. These changes can be attributed to the Pd-facilitated transformation of Fe_2O_3 to Fe_3O_4. The highly selective hydrogenation of C=C over C=O is facilitated by the flat adsorption of C=C and hindered C=O activation. The individualities and novelties of our work is as follows: (1) the novel one-pot metal free synthesis of highly robust, hydroxyl enriched, TPT-POP framework based, superior catalyst with high catalytic activity and selectivity compared to other conventional catalysts; (2) the application of spectroscopic techniques with high energy resolutions to establish useful structural-functional relationships under operando conditions; (3) elucidating of key factors affecting the catalytic activity and selectivity using *in situ* spectroscopic tools (DRIFTS/ATR-IR) that probe surface phenomena; (4) cost effective and energy efficient catalysts with outstanding magnetic recoverability (100% catalyst recovery). Our future work will be dedicated to the interface engineering and surface functionalization, through which we anticipate improvements in the catalytic performance of various challenging and attractive reactions.

Supporting Information

Characterization details, recyclability test, hot-filtration test, elemental analysis (EA), wide-angle powder XRD patterns, TGA results, TEM images, FE-SEM images, EDX spectra, XPS Spectra of O-1s & N-1s core regions, XPS survey spectra, *In situ* DRIFTS spectra, solvent effects, the influence of various catalysts used. Details of Density Functional Theory (DFT) calculations.

AUTHOR INFORMATION

Corresponding Author

*E-mail:johncuchem@gmail.com; johnmondal@iict.res.in

ORCID

John Mondal: 0000-0001-7813-2108

Quang Thang Trinh: 0000-0002-3311-4691

Wen Liu: 0000-0002-1107-131X

Notes

The authors declare no competing financial interest.

Acknowledgements:

R.P. and C.S. wish to thankfully acknowledge the DST-INSPIRE (GAP-0799) & the Council of Scientific and Industrial Research (CSIR)-University grant commission (UGC), New Delhi, for their respective junior & senior research fellowships. J.M. kindly acknowledges the Department of Science and Technology, India, for the DST-INSPIRE Faculty Research project grant (GAP-0522) at CSIR-IICT, Hyderabad. We kindly acknowledge DKIM of IICT (Division of Knowledge and Information Management) for plagiarism checking and providing them the manuscript communication number: IICT/Pubs./2020/055. J.M is also very much thankful with CSIR-YSA Research Grant with the reference no: HRDG/YSA-19/02/21(0045)/2019 for the financial support. Q.T.T., Y.Y. and W.L. acknowledge the financial support by the Singapore National Research Foundation under its Campus for Research Excellence and Technological Enterprise (CREATE) program through the Cambridge Center for Carbon Reduction in

Chemical Technology (C4T) and eCO_2EP programs. The computational work for this research is performed with the resources of the National Supercomputing Centre, Singapore (NSCC) under the project ID 12000902.

References:

1. S. Bhogeswararao, D. Srinivas, *J. Catal.* **2012**, *285*, 31–40.
2. G. Vil´e, D. Albani, A. N. Barrios, N. L´opez, J. P. Ram´ırez, *ChemCatChem***2016**, *8*, 21–33.
3. C. H. Hao, X. N. Guo, Y. T. Pan, S. Chen, Z. F. Jiao, H. Yang, X. Y. Guo, *J. Am. Chem. Soc.* **2016**, *138*, 9361-9364.
4. P. M. Arvela, J. Hajek, T. Salmi, D. Y. Murzin, *Appl. Catal. A.* **2005**, *292*, 1-49.
5. D. Verma, R. Insyani, H. S. Cahyadi, J. Park, S. M. Kim, J. M. Cho, J. W. Bae, J. Kim, *Green Chem*. **2018**, *20*, 3253-3270.
6. A. J. Plomp, H. Vuori, A. O. I. Krause, K. P. de Jong, J. H. Bitter, *Appl. Catal. A.***2008**, *351*, 9-15.
7. J. Lenz, B. C. Campo, M. Alvarez, M. Volpe, *J. Catal.* **2009**, *267*, 50.
8. J. Hajek, N. Kumar, P. M. Arvela, T. Salmi, D. Y. Murzin, I. Paseka, T. Heikkila, E. Laine, P. Laukkanen, J. Vayrynen, *Appl.Catal. A.* **2003**, *251*, 385.
9. J. P. Breen, R. Burch, J. G. Lopez, K. Griffin, M. Hayes, *Appl. Catal. A.* **2004**, *268*, 267-274.
10. C. Wang, J. S. Qiu, C. H. Liang, L. Xing, X. M. Yang, *Catal. Commun.* **2008**, *9*, 1749-1753.
11. Z. Liu, Y. Yang, J. Mi, X. Tan, Y. Song, *Catal. Commun.* **2012**, *21*, 58-62.
12. B. H. Zhao, J. G. Chen, X. Liu, Z. W. Liu, Z. Hao, J. Xiao, Z. T. Liu, *Ind. Eng. Chem. Res.***2012**, *51*, 11112−11121.
13. A. S. Nagpure, L. Gurrala, P. Gogoi, S. V. Chilukuri, *RSC Adv.* **2016**, *6*, 44333–44340.

14. Y. Yang, D. Rao, Y. Chen, S. Dong, B. WANG, X. Zhang, M. Wei, *ACS Catal.* **2018**, *8*, 11749−11760.

15. S. Fujiwara, N. Takanashi, R. Nishiyabu, Y. Kubo, *Green Chem.* **2014**, *16*, 3230–3236.

16. K. Yuan, T. Song, D. Wang, X. Zhang, X. Gao, Y. Zou, H. Dong, Z. Tang, W. Hu, *Angew. Chem. Int. Ed*. **2018**, ***57***, 5708 –5713.

17. N. Zhang, Q. Shao, P. Wang, X. Zhu, X. Huang, *Small.* **2018**, *14*, 1704318.

18. Y. Dai, X. Gao, X. Chu, C. Jiang, Y. Yao, Z. Guo, C. Zhou, C. Wan, H. Wang, Y. Yang, *J. Catal.* **2018**, *364*, 192–203.

19. K. Zhang, D. Kopetzki, P. H. Seeberger, M. Antonietti, F. Vilela, *Angew. Chem. Int. Ed.* **2013**, *52*, 1432-1436.

20. S. Dalapati, M. Addicoat, S. Jin, T. Sakurai, J. Gao, H. Xu, S. Irle, S. Seki, D. Jiang, *Nat. Commun.* **2015**, *6*, 7786.

21. P. M. Budd, B. S. Ghanem, S. Makhseed, N. B. McKeown, K. J. Msayib, C. E. Tattershall, *Chem. Commun.* **2004**, 230-231.

22. C. Gu, N. Huang, Y. Chen, L. Qin, H. Xu, S. Zhang, F. Li, Y. Ma, D. Jiang, *Angew. Chem. Int. Ed.* **2015**, *54*, 13594-13598.

23. M. Seo, S. Kim, J. Oh, S. J. Kim, M. A. Hillmyer, M. A. Hierarchically, *J. Am. Chem. Soc.***2015**, *137*, 600-603.

24. A. K. Sekizkardes, J. T. Culp, T. Islamoglu, A. Marti, D. Hopkinson, C. Myers, H. M. E. Kaderi, H. B. Nulwala, *Chem. Commun.***2015**, *51*, 13393-13396.

25. S. Dey, A. Bhunia, D. Esquivelb, C Janiak, *J. Mater. Chem. A.* **2016**, *4*, 6259-6263.

26. M. Nihei, H. Ida, T. Nibe, A. M. P. Moeljadi, Q. T. Trinh, H. Hirao, M. Ishizaki, M. Kurihara, T. Shiga, H. Oshio, *J. Am. Chem. Soc.* **2018**, *140*, 17753-17759.

27. X. Yang, B. Li, I. Majeed, L. Liang, X. Long, B. Tan, *Polym. Chem.* **2013**, *4*, 1425-1429.

28. A. Thomas, *Angew. Chem. Int. Ed.* **2010**, *49*, 8328-8344.

29. Y. Fang, X. Wang, *Angew. Chem. Int. Ed.* **2017**,*56*, 15506 – 15518.

30. V. Polshettiwar, R. S. Varma, *Org. Biomol. Chem*. **2009**, *7*, 37-40.

31. S. Mondal, S. K. Kundu, A. Bhaumik, *Chem. Commun.* **2017**, *53*, 2752–2755.

32. X. Li, M. Bao, Y. Weng, K. Yang, W. Zhang, G. Chen, *J. Mater. Chem. B.* **2014**, *2*, 5569-5575.

33. A. Tanskanen, M. Karppinen, *Sci. Rep*. **2018**, *8,* 8976.

34. X. Zhang, Y. Niu, X. Meng, Y. Li, J. Zhao, *CrystEngComm***2013**, *15*, 8166.

35. C. Cui, R. Sa, Z. Hong, H. Zhong, R. Wang, *ChemSusChem* **2020***, 13,* 180-187.

36. C. Cui, Y. Tang, M. A. Ziaee, D. Tian, R. Wang, *ChemCatChem***2018**, *10,* 1431-1437.

37. S.Mondal, J. Mondal, A. Bhaumik, *ChemCatChem***2015**,*7*, 3570-3578.

38. C. Sumathi, C. V. Raju, P. Muthukumaran, J. Wilson, G. Ravi, *J. Mater. Chem. B.* **2016**, *4*, 2561.

39. C. Sarkar, P. Koley, I. Shown, J Lee, Y. F. Liao, K. An, J. Tardio, L. Nakka, K. H. Chen, J. Mondal, *ACS Sustainable Chem. Eng.* **2019**, *7*, 10349−10362.

40. N. R. Jana, Z. L. Wang, T. Pal, *Langmuir***2000**,*16*, 2457-2463.

41. B. Guminaa, F. Mauriellob, R. Pietropaolob, S. Galvagnoa, C. Esproa, *Mol Catal***2018**, *446,* 152–160.

42. A. Vinu, K. Ariga, T. Mori, T. Nakanishi, S. Hishita, D. Golberg, Y. Bando, *Adv. Mater.* **2005**, *17*, 1648-1652.

43. Q. T. Trinh, K. Bhola, P. N. Amaniampong, F. Jérôme, S. H. Mushrif, *J. Phys. Chem. C.* **2018**, *122*, 22397-22406.

44. P. N. Amaniampong, Q. T. Trinh, K. D. O. Vigier, D. Q. Dao, N. H. Tran, Y. Wang, M. P. Sherburne, F. Jérôme, *J. Am. Chem. Soc.* **2019**, *141*, 14772-14779.

45. J. C. Wanga, J. Rena, H. C. Yaoa, L. Zhanga, J. S. Wanga, S. Q. Zanga, L. F. Hanb, Z. J. Lia, *J. Hazard. Mater*. **2016**, *311*, 11–19.

46. L. S. Shan, K. Yao, L. H. Fu, M. G. Ma, *RSC Adv.* **2016**, *6*, 2135-2140.

47. K. Dhanalaxmi, R. Singuru, S. Mondal, L. Bai, B. M. Reddy, A. Bhaumik, J. Mondal, *ACS Sustainable Chem. Eng.* **2017**, *5*, 1033-1045.

48. Y. C. Yeh, H. M. Chen, R.-S. Liu, K. Asakura, M.-Y. Lo, Y.-M. Peng, T.-S. Chan, J. F. Lee, *Chem. Mater*. **2009**, *21*, 4030-4036.

49. C. Yang, Z. Wu, G. Zhang, H. Sheng, J. Tian, Z. Duan, H. Sohn, A. J. Kropf, T. Wu, T. R. Krause, J. T. Miller, *Catal. Today.* **2019**, *323*, 123-128.

50. F. Liao, T. W. B. Lo, D. Sexton, J. Qu, C. T. Wu, S. C. E. Tsang, *Catal. Sci. Technol.* **2015**,*5*, 887-896.

51. T. Toyao, M. J. Styles, T. Yago, M. M. Sadiq, R. Riccò, K. Suzuki, Y. Horiuchi, M. Takahashi, M. Matsuoka, P. Falcaro, *CrystEngComm***2017**, *19*, 4201-4210.

52. H. Liu, Z. Li, Y. Li, *Ind.Eng. Chem. Res.* **2015**, *54*, 1487-1497.

53. Y. Yang, D. Rao, Y. Chen, S. Dong, B. Wang, X. Zhang, M. Wei, *ACS Catal.* **2018**, *8*, 11749-11760.

54. R. Gao, L. Pan, H. Wang, Y. Yao, X. Zhang, L. Wang, J. J. Zou, *Adv. Sci.* **2019**, *6*, 1900054.

55. Q. T. Trinh, B. K. Chethana, S. H. Mushrif, *J. Phys. Chem. C.* **2015**, *119*, 17137-17145.

56. L. J. Durndell, C. M. A. Parlett, N. S. Hondow, M. A. Isaacs, K. Wilson, A. F. Lee, *Sci. Rep.* **2015**, *5*, 9425.

57. M. Jiang, N. Koizumi, M. Yamada, *J. Phys. Chem. B.* **2000**, *104(32)*, 7636-7643.

58. Q. T. Trinh, J. Yang, J. Y. Lee, M. Saeys, *J. Catal.* **2012,** *291*, 26-35.

59. S. Chen, L. Meng, B. Chen, W. Chen, X. Duan, X. Huang, B. Zhang, H. Fu, Y. Wan, *ACS Catal*. **2017**, *7(3)*, 2074-2087.

60. C. Xu, D. W. Godman, *Langmuir***1996**, *12*, 1807-1816.

61. H. Liu, Z. Li, Y. Li, *Ind.Eng. Chem. Res.* **2015**, *54*, 1487-1497.

62. Y. Yang, D. Rao, Y. Chen, S. Dong, B. Wang, X. Zhang, M. Wei, *ACS Catal.* **2018**, *8*, 11749-11760.

63. R. Gao, L. Pan, H. Wang, Y. Yao, X. Zhang, L. Wang, J. J. Zou, *Adv. Sci.* **2019**, *6*, 1900054.

64. L. J.Durndell, C. M. A.Parlett, N. S.Hondow, M. A.Isaacs, K.Wilson, A. F. Lee, *Sci. Rep.* **2015**, *5*, 9425.

65. M. Jiang, N. Koizumi, M. Yamada, *J. Phys. Chem. B.* **2000**, *104*, 7636-7643.

66. S. Chen, L. Meng, B. Chen, W. Chen, X. Duan, X. Huang, B. Zhang, H. Fu, Y. Wan, *ACS Catal.* **2017**,*7*, 2074-2087.
67. F. Delbecq, P. Sautet, *J. Catal*. **1995**, *152*, 217.
68. Y. Zhang, C. Chen, W. Gong, J. Song, Y. Su, H. Zhang, G. Wang, H. Zhao, *RSC Adv*. **2017**,*7*, 21107-21113.
69. J. Yu, L. Yan, G. Tu, C. Xu, X. Ye, Y. Zhong, W. Zhu, Q. Xiao, *Catal Lett* **2014**, *144*, 2065-2070.
70. S. C. Shit, P. Koley, B. Joseph, C. Marini, L. Nakka, J. Tardio, J. Mondal, *ACS Appl. Mater. Interfaces***2019**, *11*, 24140-24153.
71. J. Yu, L. Yan, G. Tu, C. Xu, X. Ye, Y. Zhong, W. Zhu, Q. Xiao, *CatalLett***2014**, *144*, 2065-2070.
72. G. Kresse, J. Hafner, *Phys. Rev. B* **1993**, *47*, 558-561.
73. G. Kresse, J. Furthmüller, *Comput.* **1996,** *6*, 15-50.
74. J. Klimeš, D. R. Bowler, A. Michaelides, *J. Condens*. **2009,***22*, 022201.
75. J. Klimeš, D. R. Bowler, A. Michaelides, *Phys. Rev. B* **2011**, *83*, 195131.
76. Q. Mohan, Q. T. Trinh, A. Banerjee, S. H. Mushrif, *MolSimulat**2019,** 45*, 1163-1172.
77. Q. T. Trinh, A. V. Nguyen,D. C. Huynh, T. H. Pham, S. H. Mushrif, *Catal. Sci. Technol.***2016**,*6*, 5871-5883.
78. H. Yildirim, A. Kara, *J. Phys. Chem. C* **2013**, *117*, 6, 2893-2902.
79. J.Carrasco, W. Liu, A. Michaelides, A. Tkatchenko, *J. Chem. Phys. **2014**, 140*, 084704.
80. C. Sarkar, S. C. Shit, D. Q. Dao, J. Lee, N. H. Tran, R. Singuru, K. An, D. N. Nguyen, Q. V. Le, P. N. Amaniampong, A. Drif, F. Jerome, P. T. Huyen, T. T. N. Phan, D. V. N. Vo, N. T. Binh, Q. T. Trinh, M. P. Sherburne, J. Mondal, *Green Chem.***2020,** *22*, 2049-2068.
81. H. Asakawa, S. Matsui, Q. T. Trinh, H. Hirao, Y. Inokuma, T. Ogoshi, S. Tanaka, K. Komatsu, A. Ohta, T. Asakawa, T. Fukuma, *J. Phys. Chem. C.* **2020.**
82. J. Mondal, Q. T. Trinh, A. Jana, W. K. H. Ng, P. Borah, H. Hirao, Y. Zhao, *ACS Appl. Mater. Interfaces* **2016**, *8*, 15307-15319.
83. H. Yildirim, T. Greber, A. Kara, *J. Phys. Chem. C.* **2013**, 117, 20572-20583.
84. F. Zaera, *ACS Catal.* **2017,***7*, 4947-4967.
85. R. Singuru, Q. T. Trinh, B. Banerjee, B. G. Rao, L. Bai, A. Bhaumik, B. M. Reddy, H. Hirao, J. Mondal, *ACS Omega* **2016**, *1*,1121-1138.

86. C. Sarkar, S. Pendem, A. Shrori, D. Q. Dao, P. P. T. Mai, T. N. Ngoc, D. R. Chandaka, T. V. Rao, Q. T. Trinh, M. P. Sherburne, J. Mondal, *ACS Appl. Mater. Interfaces* **2019,***11,* 11722-11735.
87. Q. T. Trinh, A. Banerjee, Y. Yang, S. H. Mushrif, *J. Phys. Chem. C* **2017,***121,* 1099-1112.
88. J. C. S. Ruiz, A. L. Cudero, J. S. Gullón, A. S. Escribano, A. Aldaz, F. R. Reinoso, *J. Catal.* **2008**, *253,* 159-166.
89. Z. C. Zhang, X. Zhang, Q. Y. Yu, Z. C. Lui, C. M. Xu, J. S. Gao, J. Zhuang. X. Wang, *Chem. Eur. J.* **2012,***18,* 2639 – 2645.
90. T. Birchem, C. M. Pradier, Y. Berthier, G. Cordier, *J. Catal*. **1996,***161,* 68–77.
91. G. T. K. K. Gunasooriya, E. G. Seebauer, M. Saeys, *ACS Catal.* **2017**, *7,* 3, 1966-1970.

Graphical Abstract:

Porous-Organic-Polymer-Triggered Advancement of Sustainable Magnetic Efficient Catalyst for Chemoselective Hydrogenation of Cinnamaldehyde

Porous-Organic-Polymer (POP) encapsulated magnetic catalyst (Pd-Fe_3O_4) exhibited advancement in chemoselective hydrogenation of Cinnamaldehyde (CAL) to Hydrocinnamaldehyde (HCAL, 100% selectivity), which could be attributed to the formation of Pd-Fe bond with the decrease of Pd-Pd bond distance and flat adsorption of C=C on the Pd surface followed by the contraction of C=O bond as experimentally evidenced with the combination of synchrotron based EXAFS analysis & in-situ ATR-IR, DRIFTS spectroscopy studies.